The Tiger Deposit: A Carbonate-Hosted, Magmatic-Hydrothermal Gold Deposit, Central Yukon, Canada

Eric J. Thiessen,[1,†] Sarah A. Gleeson,[1] Venessa Bennett,[2] and Robert A. Creaser[1]

[1] *University of Alberta, Department of Earth and Atmospheric Sciences, Edmonton, Alberta T6G 2E3, Canada*

[2] *Geomantia Consulting, 33 Roundel Road, Whitehorse, Yukon Y1A 3H4, Canada*

Abstract

The Tiger gold deposit, located in central Yukon, Canada, has an inferred resource of 8.28 Mt containing 289,400 ounces gold at an average grade of 1.09 g/t and an indicated resource of 7.15 Mt containing 509,000 ounces gold at an average grade of 2.21 g/t. A detailed paragenetic and geochemical study of the carbonate-hosted replacement-style deposit provides constraints on the fluid history and genesis of the gold mineralizing system. The deposit is hosted in Silurian-Devonian unmetamorphosed carbonate rocks of the Mackenzie Platform and occurs 7 km northeast of the Dawson thrust, which broadly marks the northeast boundary of the Selwyn Basin. A nearby Paleocene intrusion, the Rackla pluton, subcrops ~3 km from the Tiger deposit. No other deposits of this kind have been described within the Mackenzie Platform. The Tiger deposit consists of strata-bound replacement-style mineralization adjacent to an interpreted local feeder fault. Mineralization occurs in two distinct assemblages: (1) hydrothermal dolomite, gold-bearing arsenopyrite, and minor pyrite and (2) fractures hosting native gold associated with bismuth, antimony, silver, tungsten, and minor base metals.

Carbon, oxygen, and strontium isotope values suggest magmatic water, originating from the Rackla pluton, as the source of mineralizing fluids for the Tiger deposit. Microthermometric data from gold-bearing dolomites, quartz, and sphalerite document the presence of hot, ~350°C aqueous-carbonic fluids for the duration of gold mineralization, overprinted by cooler, ~150°C aqueous meteoric fluids late in the paragenesis during the waning of the mineralizing system. The Tiger deposit is thus interpreted to represent a distal expression of Paleocene magmatic activity hosted in carbonates northeast of the Selwyn Basin, central Yukon.

Introduction

The Tiger carbonate-hosted gold deposit, located in central Yukon, Canada (Fig. 1), has an inferred resource of 8.28 Mt containing 289,400 ounces gold at an average grade of 1.09 g/t and an indicated resource of 7.15 Mt containing 509,000 ounces gold at an average grade of 2.21 g/t (Stroshein et al., 2011). The deposit is hosted by Paleozoic platform carbonates and is characterized by pervasive strata-bound carbonate-replacement gold mineralization that manifests as a mineral assemblage of dolomite and gold-bearing arsenopyrite, free gold in fractures, and gold-rich oxide mineralization. Oxide mineralization overprints and lies structurally above the dolomite mineralization.

Only two other carbonate-hosted gold deposits are documented in the Yukon, the past-producing Ketza River oxide gold deposit in southeast Yukon and the Nadaleen prospects 100 km east of the Tiger. Stroshein (1996) and Fonseca (1998) have suggested that Ketza River may be an example of a gold-rich, base metal-poor manto-type deposit. These are oxidized, replacement deposits formed by high-temperature (>300°C) hydrothermal fluids related to porphyries. In contrast, the Nadaleen prospects are considered analogous to the Carlin-type carbonate-hosted disseminated gold deposits of Nevada (Tucker, 2015); they are gold-bearing, structurally controlled, replacement-style systems within Ediacaran sedimentary rocks of the Selwyn Basin (Moynihan, 2013). Preliminary work has constrained the age of mineralization between 74 and 42 Ma (Tucker, 2015); however, no clear link between magmatic activity and the mineralization has been demonstrated.

The Tiger deposit occurs on the margin of a prospective gold belt, the Tintina gold province of the northern Cordillera of Alaska and the Yukon (Fig. 1), which is host to a distinct class of gold occurrences, the intrusion-related gold deposits (IRGDs—Thompson et al., 1999; Lang and Baker, 2001; Hart, 2007). Globally, these gold-bearing systems are commonly but not exclusively characterized by sheeted quartz vein systems that are associated with (1) metaluminous, subalkalic felsic to intermediate intrusions, (2) carbonic hydrothermal fluids, (3) a base metal poor-assemblage of Bi, W, As, Mo, Te ± Sb ± Au, (4) a reduced ore assemblage of arsenopyrite, pyrrhotite, pyrite, and minor magnetite, (5) areally restricted and weak hydrothermal alteration halos, (6) a tectonic setting well inboard of convergent plate boundaries, and (7) magmatic W and Sn provinces (Lang and Baker, 2001). Additionally, it has been suggested that these systems only occur in metamorphosed pericratonic terranes such as the Selwyn Basin and do not occur in platformal sequences such as the Mackenzie Platform (Hart, 2007). In the northern North American Cordillera these deposits predominantly occur in a belt within the Tintina gold province, the Tombstone-Tungsten magmatic belt, which is situated southwest of the Tiger deposit (Fig. 1). The mid-Cretaceous (97–90 Ma) Tombstone-Tungsten magmatic belt comprises the Tombstone, Mayo, and Tungsten intrusive suites (Hart et al., 2004), all of which intrude nonplatformal autochthonous rocks inboard of the accreted allochthonous terranes (Mair et al., 2006b). A volumetrically minor plutonic suite, the McQuesten suite, with ages of 66.8 to 64.0 Ma (Murphy, 1997), occurs within the western Tombstone-Tungsten magmatic belt and has not been considered prospective for gold thus far (Murphy, 1997). The two best known examples of mid-Cretaceous IRGDs are the Fort Knox
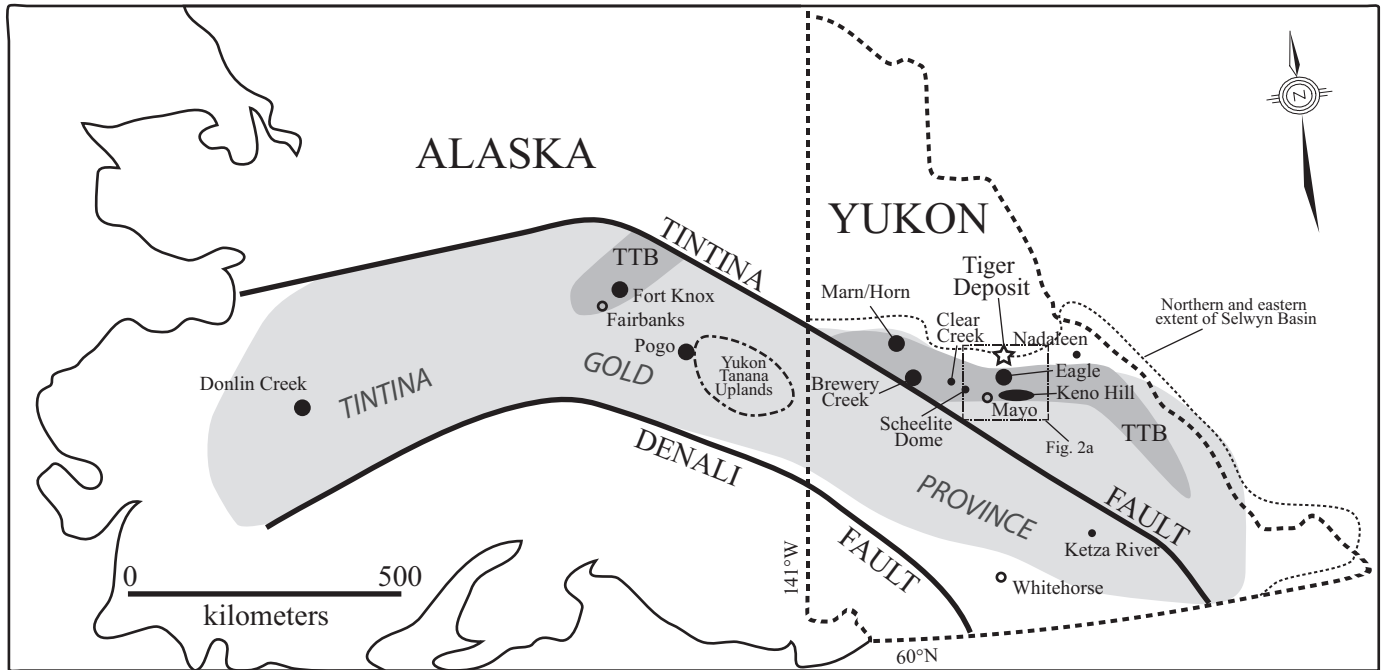
Fig. 1. The northern Cordillera of Yukon and Alaska, highlighting the Tintina gold province, Tombstone-Tungsten magmatic belt (TTB), and associated intrusion-related gold deposits (modified from Hart, 2007).

gold mine, owned and operated by Kinross Gold Corp. and located near Fairbanks, Alaska, and the Eagle gold deposit (Fig. 1), an advanced-stage project operated by Victoria Gold Corp occurring ~50 km southwest of the Tiger deposit, near Keno City, central Yukon (Maloof et al., 2001; Stephens et al., 2004; Hart, 2007).

This study was undertaken to describe the geochemistry and fluid evolution pertaining to gold deposition within the Tiger deposit. Because no similar styles of mineralization have yet been described in this part of the Yukon, an additional objective of this study is to determine whether mineralization is linked to the well-described IRGD systems or a distinct mineralizing style. Although the oxide mineralization contains appreciable amounts of gold, it is not amenable to a geochemical description using the techniques applied herein and is thus not discussed in any detail.

Regional Geology and Tectonic Setting

The Tiger deposit is situated in the Jurassic-Cretaceous fold and thrust belt of the northern North American Cordillera at the boundary of autochthonous rocks of the Selwyn Basin and the Mackenzie Platform (Fig. 1; Abbott et al., 1986). Gabrielse (1967) defines the Selwyn Basin as a passive margin succession (shelf, slope, and basinal strata) that accumulated on the western border of ancient North America from the Neoproterozoic to Jurassic. Most of the northwestern Selwyn Basin consists of slope to basin facies coarse quartz sandstone, shale, and carbonates (Gordey and Anderson, 1993; Murphy, 1997). Rifting in the Early to Middle Devonian caused the western continental margin of North America to form the Slide Mountain Ocean, which isolated the now parautochthonous Yukon Tanana terrane from the autochthonous Selwyn Basin (Mortensen, 1992; Mair et al., 2006b). As

a result, within the Selwyn Basin the Earn Group was deposited in a series of fault-bounded basins developed within a now restricted deep marine setting, forming complex internal stratigraphy (Gordey et al., 1991). This period of subsidence and subsequent rifting in the Selwyn Basin also resulted in episodic volcanism and correlative shale-hosted Pb-Zn deposits (Gordey and Anderson, 1993; Murphy, 1997).

Platform carbonates and sediments of the Mackenzie Platform were deposited during the Proterozoic and Paleozoic roughly northeast (present day) of the Selwyn Basin. Mackenzie platform sediments consist of the Proterozoic Wernecke Supergroup, Pinguicula Supergroup, Mackenzie Mountains Supergroup, and Windermere Supergroup (Aitken and McMechan, 1992; Narbonne and Aitken, 1995). Paleozoic shelf carbonate rocks of the Bouvette Formation occur within the immediate study area, are the host to the Tiger deposit mineralization, and are broadly described as a Cambrian to Devonian sedimentary package consisting of platformal limestones and dolostones (Morrow et al., 1999).

Deformation of these basinal and platformal rocks commenced during the Late Triassic when regional northeasterly directed compression imbricated and folded the strata (Murphy, 1997). The most intense deformation occurred southwest of the Selwyn Basin and Mackenzie Platform within the parautochthonous Yukon Tanana terrane as it converged with North America (Mair et al., 2006b). The Early Jurassic to Early Cretaceous compression produced a series of large-scale, pervasive thrust fault systems (Fig. 2) in the Selwyn Basin and Mackenzie Platform foreland (Abbott et al., 1986). The largest displacements occur along the Robert Service thrust and the Tombstone thrust, with little documented displacement along the Dawson thrust (Mair et al., 2006b). The Dawson thrust, which broadly separates Selwyn Basin rocks
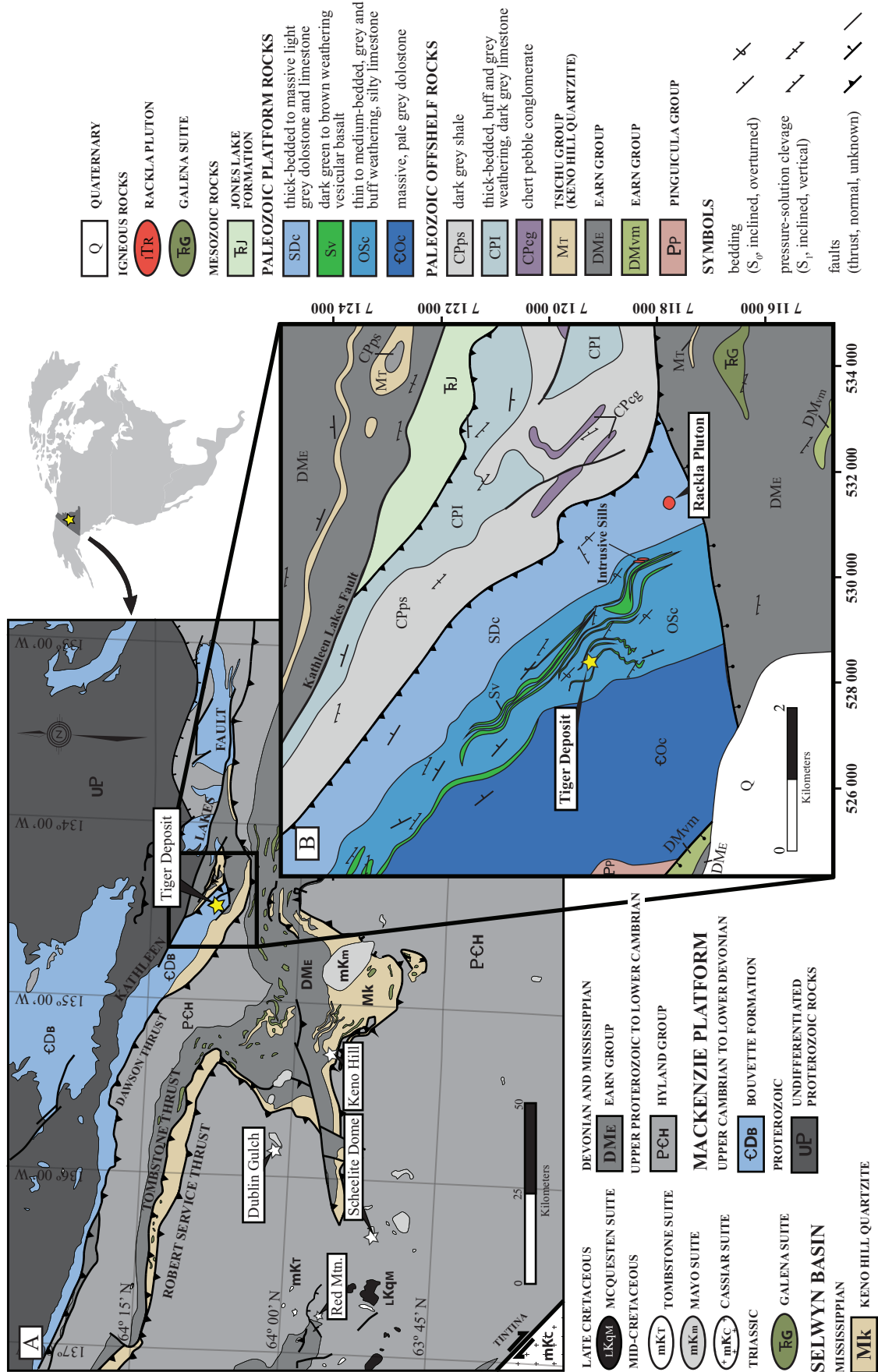
Fig. 2. A) Regional geology of the northwestern Selwyn Basin, including the Tiger deposit and various Cretaceous intrusive occurrences and deposits (modified from Gordey and Makepeace, 2001). B) Local geology of the study area. Coordinates are in UTM NAD83, zone 8 (modified from Colpron et al., 2013).

to the southwest (hanging wall) from Mackenzie Platform rocks to the northeast (footwall; Murphy, 1997), occurs ~7 km southwest of the Tiger deposit, which sits in the footwall of the thrust (Fig. 2). Uplift and extension are documented within the Yukon Tanana Uplands of Alaska (Hudson, 1994); however, similar geologic interpretations have not been made for the Selwyn Basin and Mackenzie Platform, which is reflected by the relative lack of mid-Cretaceous plutonism therein (Mair et al., 2006b). Following the major episode of crustal thickening and deformation, dextral strike-slip motion initiated on the Tintina fault at about 85 Ma due to the newly established northward-directed subduction of the Kula plate (Engebretson et al., 1985).

Intrusive rocks in the study area (Figs. 2, 3) include the mid-Cretaceous 95 to 92 Ma Mayo suite (Hart et al., 2004) and the 92 to 90 Ma Tombstone suite, as well as the Late Cretaceous to early Paleocene 66.8 to 64.0 Ma McQuesten suite (Murphy, 1997). The Mayo suite rocks are composed dominantly of metaluminous, coarse-grained leucocratic quartz monzonite, granodiorite, and biotite granite (Murphy, 1997). These ilmenite-series intrusions have initial strontium isotope values ($^{87}Sr/^{86}Sr$) of 0.710 to 0.730, indicating assimilation of crustal rocks with high $^{87}Rb/^{86}Sr$, probably sedimentary in origin (Hart et al., 2004). Mineral occurrences associated with Mayo suite intrusive rocks include the Dublin Gulch (Eagle deposit), Scheelite Dome, and Clear Creek gold deposits (Figs. 1, 2; Murphy, 1997; Hart et al., 2004; Mair et al., 2006a). The Keno Hill district Ag-Pb-Zn vein deposits are also in close proximity to these intrusions, yet a genetic link between the two has not been clearly demonstrated (Lynch et al., 1990). Tombstone intrusive rocks range in composition from metaluminous monzonite to granodiorite to syenite (Murphy, 1997). These intrusions commonly are magnetite

bearing, have high initial $^{87}Sr/^{86}Sr$ values of 0.710, and have Au-Cu-Bi skarn occurrences (e.g., Marn and Horne; Brown and Nesbitt, 1987; Murphy, 1997) and IRGD mineralization (e.g., Brewery Creek; Baker and Lang, 2001; Lang and Baker, 2001; Hart, 2007). McQuesten suite intrusions (Fig. 2) comprise peraluminous biotite-muscovite granite and quartz monzonite compositions and have very few associated mineral occurrences (Murphy, 1997).

Local Geology and Field Relationships

The Tiger deposit is hosted by the Bouvette Formation, which comprises bedded limestones intercalated with locally extensive basalt flows and airfall tuffs, all of which dip to the northeast (Figs. 4, 5). The Bouvette Formation locally consists of lime mudstone to skeletal wackestone with minor skeletal floatstone and rudstone. Primary fossil assemblages include crinoid ossicles, rugose corals, bryzoans, stromatoporoids, and the tabulate corals *Favosites favosus*, *Halysites catenularia*, and *Syringopora flexuosa*. This suggests the limestone hosting the Tiger deposit is Silurian in age (Moore et al., 1952) and is in agreement with Abbott (1990), who classified this unit as being Ordovician to Silurian in age. Way-up indicators (ripple laminations) suggest the rocks young to the northeast. There is also an apparent northeastward shallowing of the depositional environment from basal terrigenous mudstone to the southwest and carbonate turbidites to upper ramp or lagoonal facies to the northeast (E.C. Turner, pers. comm., 2010). The intercalated volcanic rocks on the property have not been dated, but, given the Ordovician to Silurian age of the limestones, they may belong to the Marmot Formation described in eastern Yukon and western Northwest Territories within the Mackenzie Mountains and Misty Creek Embayment (Goodfellow et al., 1995; Leslie, 2009).
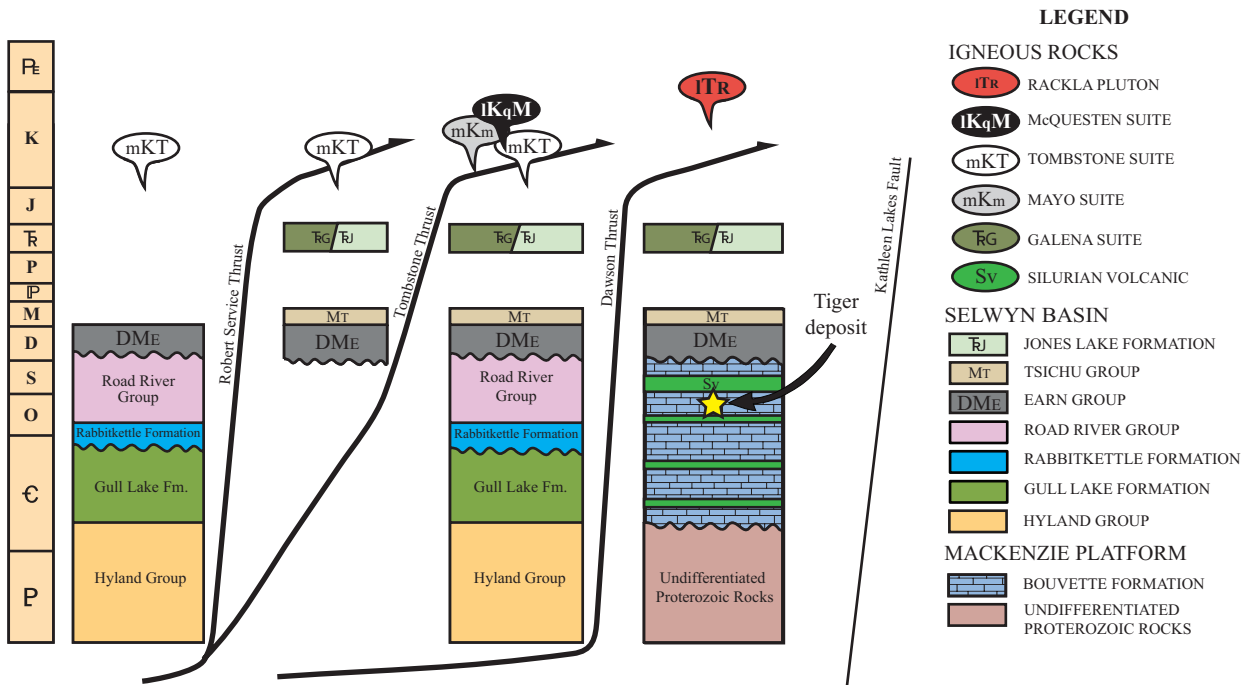
Fig. 3. Generalized regional stratigraphy surrounding the Tiger deposit and northwestern Selwyn Basin, categorized by specific thrust-sheet packages (modified from Murphy, 1997).
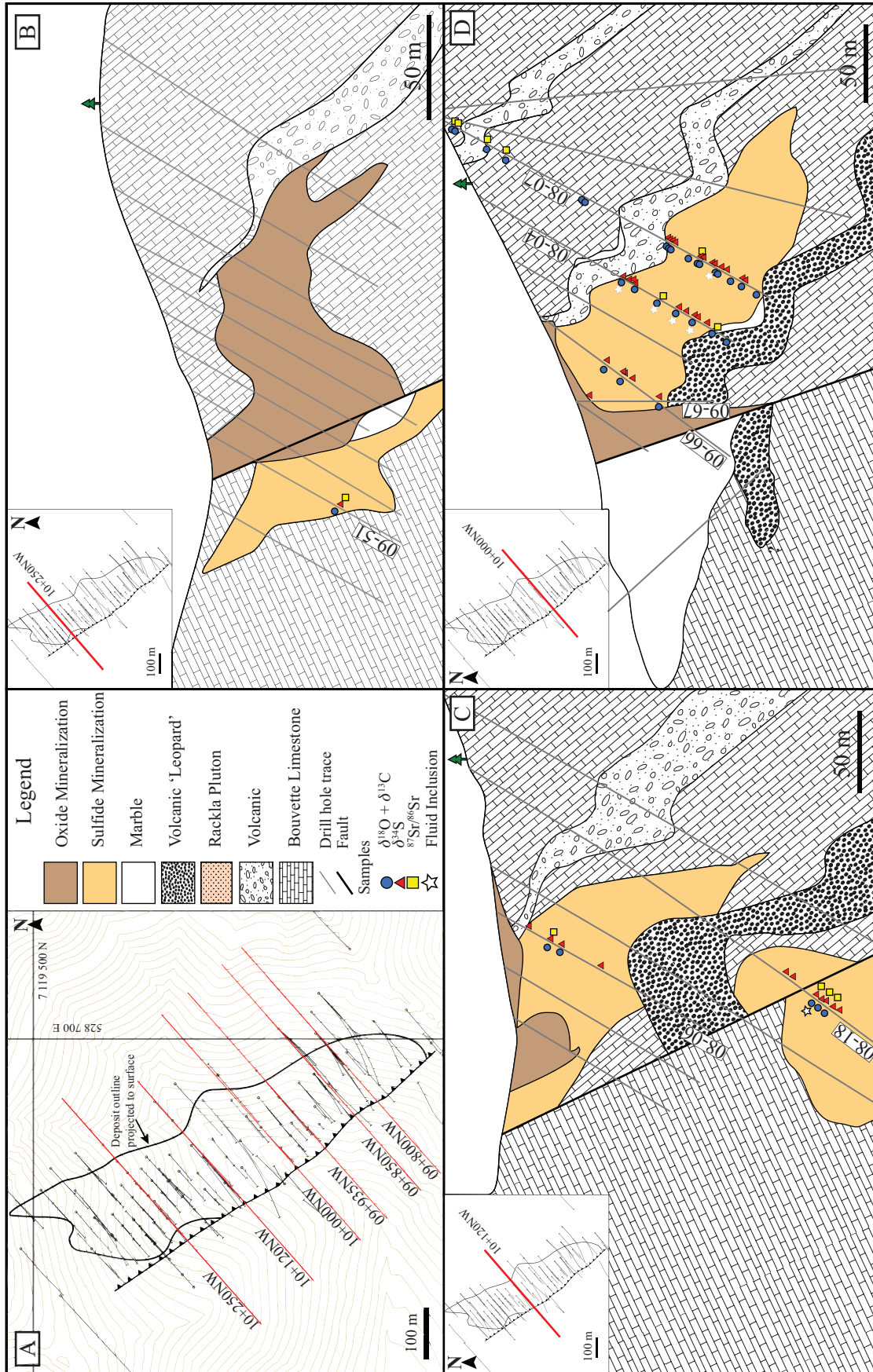
Fig. 4. Tiger deposit drill area and cross sections with sample locations. All cross sections are southwest to northeast (left to right) and select drill traces have labeled drill hole numbers. A) Plan view drill map of the Tiger deposit with orebody outline projected to surface and representative cross section traces. B) Section 10+250NW. C) Section 10+120NW. D) Section 10+100NW.

Fig. 5. Tiger deposit cross sections with sample locations. All cross sections are southwest to northeast (left to right), except for Sc10-05, which is south to north. Select drill traces have labeled drill hole numbers. A) Section 9+935NW. B) Section 9+850NW. C) Section 9+800NW. D) South to north cross section of drill hole Sc10-05 that intersects the Rackla pluton ~3 km east of the Tiger deposit. Refer to Figure 4 for Legend.
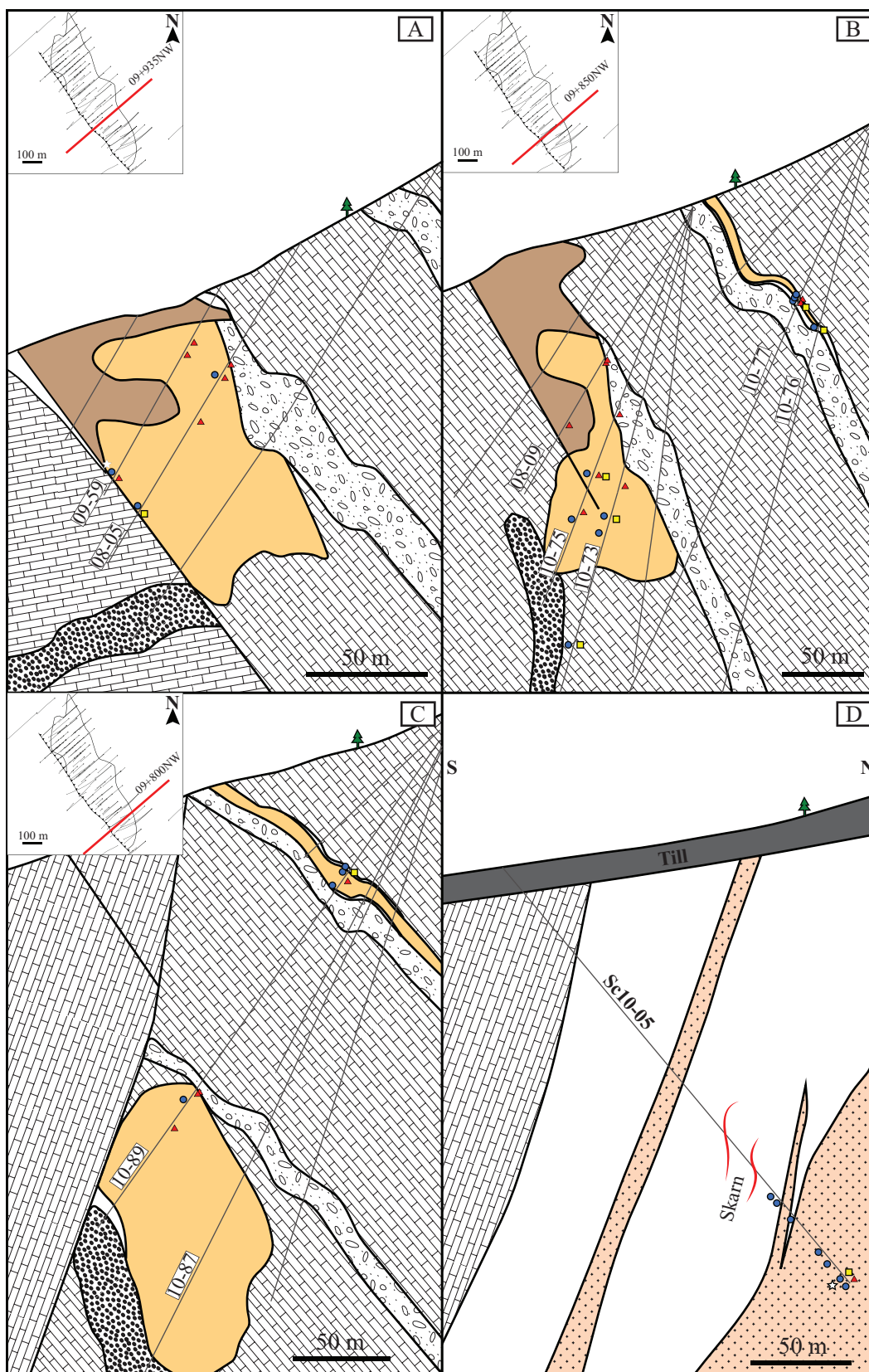
A two-mica granite, the Rackla pluton, intrudes Bouvette Formation stratigraphy ~3 km east-southeast of the Tiger deposit and manifests as a subcropping stock (Fig. 5). Small aplitic and pegmatitic dikes and sills also occur ~2 km east of the Tiger deposit and have yielded ^{40}Ar/^{39}Ar muscovite ages of 62.3 ± 0.7, 62.4 ± 1.8, and 59.1 ± 2 Ma (Kingston et al., 2010). No intrusive rocks have been found within the immediate Tiger deposit at surface or in drill core.

Mineralization is constrained mostly within an NW-trending 600- × 200- × 80-m-deep zone hosted in a carbonate unit, the Discovery Horizon, which is bounded to the top (northeast) and bottom (southwest) by volcanic units (Figs. 4, 5) within an NW-trending property-scale shear zone. The intercalated volcanic-carbonate package is truncated to the southwest by an NW-trending, high-angle fault—the Tiger fault (Figs. 4, 5). Sulfide mineralization also occurs in the Upper Horizon, adjacent to a volcanic unit stratigraphically above the main Discovery Horizon (Fig. 5b, c).

The high-angle Tiger fault, which bounds mineralization to the southwest, truncates a thick sequence of deformed white marble in the immediate footwall and a distinctive volcaniclastic unit informally termed the "leopard unit" in the hanging wall (Figs. 4, 5). The leopard unit is distinctive from other volcanic rocks due to its high calcite content (>50%) of unclear origin.

Regional exploration within 5 km of the Tiger deposit has resulted in the discovery of several polymetallic quartz veins ± gold, scheelite-bearing tremolite skarn, pyrrhotite ± scheelite ± chalcopyrite-bearing actinolite-diopside-garnet skarn, and wolframite ± tantalite occurrences. Three scheelite-tremolite-actinolite skarn showings occur between the Tiger deposit and the Rackla pluton within the Bouvette Formation. The most strongly altered skarn occurrences are associated with SW-striking quartz-muscovite-pegmatitic dikes. Geochemical anomalies for these skarns include elevated tungsten, gold, and rare copper (Dumala, 2010).

Analytical Methods

Petrography

Over 600 hand samples and 100 thin sections were analyzed throughout the deposit in order to adequately constrain mineral paragenesis, outlined in Figure 6. Thin section petrography, benchtop-based cathodoluminescence (CL), and electron microprobe analyses (EPMA) with a Cameca SX 100 were utilized at the University of Alberta to construct the paragenetic sequence. The EPMA beam operated at an accelerating voltage of 20 kV, a probe current of 20 nA, and a beam diameter of 1 μm.

Whole-rock analysis

Thirteen samples of the Rackla pluton were analyzed by ALS Global in Vancouver, British Columbia, for major element lithogeochemistry by fused disc X-ray fluorescence (XRF) spectroscopy and ferrous iron by titration. Two internal reference materials, a blank and a duplicate sample, were analyzed for quality assurance.
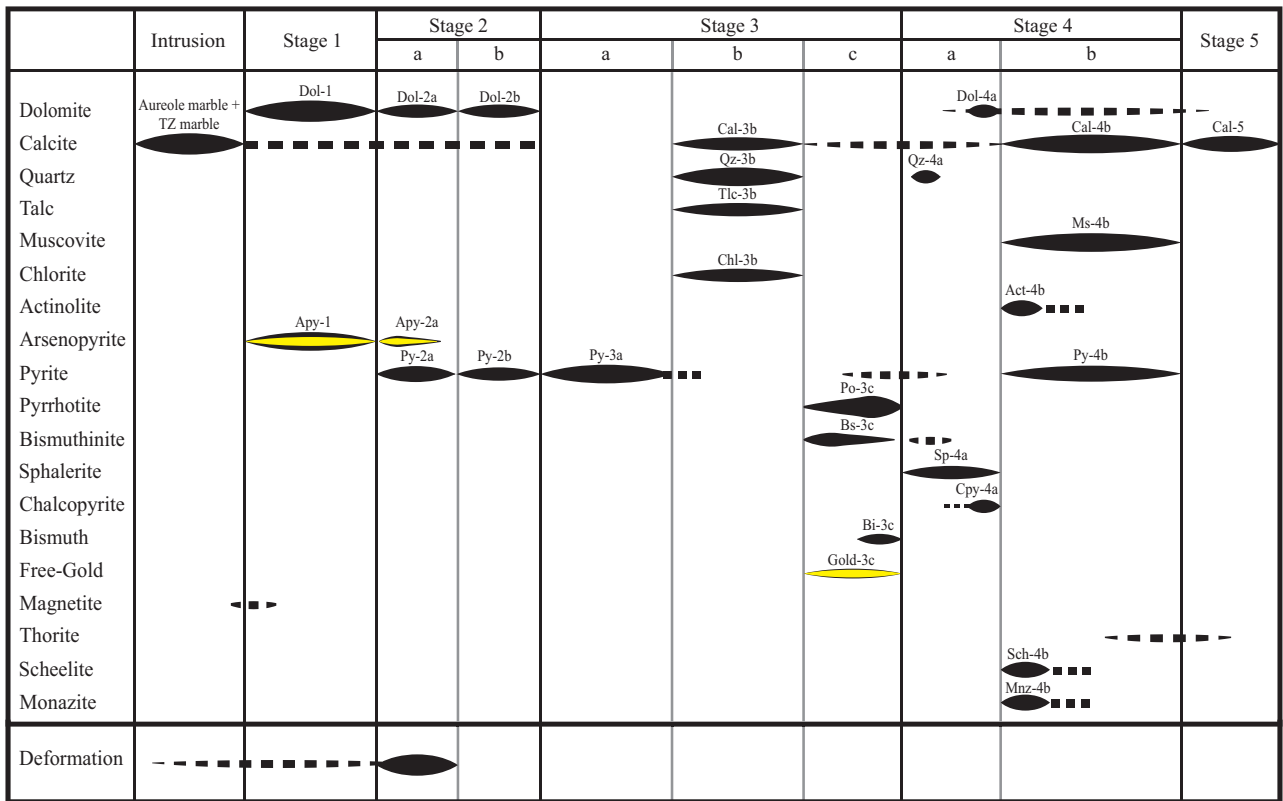

Fig. 6. Paragenetic sequence of the Tiger deposit mineralization. Line thickness indicates approximate relative mineral abundance and dashed lines are inferred occurrences.

Microthermometry

All microthermometry was performed on a Linkam THMSG600 heating/freezing stage mounted on an Olympus BX50 microscope. The heating/freezing stage has a working range of –196° to 600°C. Calibration at –56.6° (pure CO_2), 0°, and 374.1°C using synthetic fluid inclusion standards from SynFlinc was completed before and after microthermometry. Accuracy below 0°C is ±0.2°C and, above 0°C, accuracy is ±2°C. Reported salinities have been calculated using equations from Bodnar (1993) for ice melting and Sterner et al. (1988) for halite dissolution temperatures. The H_2O-NaCl model system is used due to the eutectic melting range (–22 to –40°C); thus, salinities are reported in wt % NaCl equiv.

Stable isotopes: Carbon, oxygen, and sulfur

Carbon and oxygen stable isotope analyses of carbonates were completed at the Isotope Science Lab, Department of Physics and Astronomy, University of Calgary. Using lab standards (NBS 18, NBS 19, IAEA CO-1, IAEA CO-8, IAEA CO-9), the sample analyses are reported to be precise and accurate to 0.2‰ (1σ) for $\delta^{13}C$ and $\delta^{18}O$ values. Whole-rock Rackla pluton and Tiger deposit quartz (quartz 3b) samples were also analyzed for oxygen isotope values at the University of Alberta's Stable Isotope Laboratory. These samples were measured based on the methodology of Clayton and Mayeda (1963). Analyses are precise to 0.4‰ (2σ) and reported relative to Vienna-Standard Mean Ocean Water (V-SMOW). Sulfur isotope analysis was conducted on pure sulfide mineral separates and analyzed at the Isotope Science Laboratory, Department of Physics and Astronomy, University of Calgary, by the method described by Glesemann et al. (1994). Using lab standards (IAEA S1, IAEA S2, IAEA S3), the precision and accuracy at 1σ (n = 10) is 0.3‰.

Strontium isotopes

Strontium isotope analyses were performed in a class 100 cleanroom in the Radiogenic Isotope Facility (RIF), University of Alberta, following the methods described in Buzon et al. (2007). Internal precision (error) of an individual strontium isotope ratio varies from 0.00001 to 0.00014 (2σ level).

Results

Petrography and paragenesis

Host rock: The carbonate host rocks of the Bouvette Formation range from lime mudstones and dolomudstones (Fig. 7a) to crinoidal packstones and coral rudstones. The host carbonates are dark gray in color and contain opaque material in thin section (10–50% of the rock) as well as extensive single-seam stylolites that form subparallel to bedding. The carbonates are brecciated within the deposit and regionally throughout the Bouvette Formation. The most common breccia type is a mosaic breccia with polyphase cements beginning with a 1-cm-long "dog tooth" dolomite spar that crystallizes on limestone clasts (Fig. 7a). This dolomite is rimmed by a thin veneer of submillimeter-sized tabular pyrobitumen (Fig. 7a) and subsequent infilling is composed of quartz and calcite with minor fine-grained pyrite.

The host rocks contain 10- to 30-m-thick volcanic flows, tuffs, and epiclastic rocks that have sharp, interbedded contacts with host-rock carbonates. The volcanic rocks are commonly fine grained and layered. The layering may be of primary volcanic origin but also may be a deformational feature. One of the most identifiable units is a black amygdaloidal basalt that contains calcite-filled amygdules. Beds of lapilli tuff with graded bedding occur locally within the volcanic units. Additionally, magnetite-bearing pebble to cobble conglomeratic volcanic rocks occur with locally high concentrations of magnetite, ~20% in centimeter-scale intervals.

Rackla pluton and marble: The Rackla pluton contains 10 to 50% quartz, 30 to 60% K-feldspar, and 10 to 60% plagioclase feldspar and, therefore, has compositions ranging from granite to quartz monzonite to granodiorite (Fig. 7b). Primary biotite and muscovite phases are minor components (<5%) of the rock. Crystals are commonly 0.5 to 1 cm in diameter, but some plagioclase megacrysts are 3 to 4 cm long. The most common texture consists of centimeter-scale blocky to interlocking equant grains of quartz and feldspar; however, meter-scale portions may be granophyric to pegmatitic with graphic granite textures present. Plagioclase in least-altered drill core has a chalky appearance, whereas more altered portions of the rock appear green and contain abundant sericite, epidote, and chlorite (Fig. 7b). Carbonate veins with bleached halos crosscut the intrusion. Minor fine-grained euhedral pyrite, arsenopyrite, and sphalerite occur disseminated throughout the intrusive rock, with higher sulfide concentrations occurring proximal to crosscutting calcite and dolomite veins (Fig. 7b). A contact metamorphic aureole of marble surrounds the Rackla pluton and can be traced in drill core for ~150-m apparent thickness. Drilling intersected a centimeter- to meter-scale actinolite skarn in one drill hole at the contact of the aureole marble and unmetamorphosed limestone. This unit is dark green in color, has a fibrous texture, and contains minor sulfides such as pyrite and pyrrhotite.

Rackla pluton samples have been classified for alumina saturation using major element oxides. All samples have Al_2O_3 molar proportions that exceed combined CaO + K_2O + Na_2O molar proportions (Table 1), indicating the pluton is weakly peraluminous. Additionally, Rackla pluton samples have ferric/ferrous iron values below 0.5 at 70 wt % SiO_2 (Fig. 8), and are therefore classified as ilmenite series or reduced affinity using the classification of Ishihara et al. (2000).

Tiger marbles: The host-rock limestone has also been transformed to marble locally within the Tiger deposit (Fig. 7c) and in the footwall of the Tiger fault. This marble is very fine grained, sucrosic, and disaggregates with only minor handling. Marble in the Tiger fault shows abundant shear fabrics. Other marble commonly occurs at the upper and lower boundaries between volcanic horizons and limestone rocks above and within the Discovery Horizon and proximal to the Tiger fault (Figs. 4, 5). The thickness of this marble can reach ~100 m (stratigraphic orientation unknown) in the sheared footwall of the Tiger fault; however, 1- to 4-m intersections are more common adjacent to volcanic units. The contacts between the marbles and limestones are mostly gradational and interbedded on the centimeter scale. Similarly, the contacts of the marbles and the volcanic horizons are also gradational. The volcanic unit basal to the Discovery Horizon contains over 50% calcite for depths of a few meters to hundreds of meters and is informally known as the leopard unit, as it has
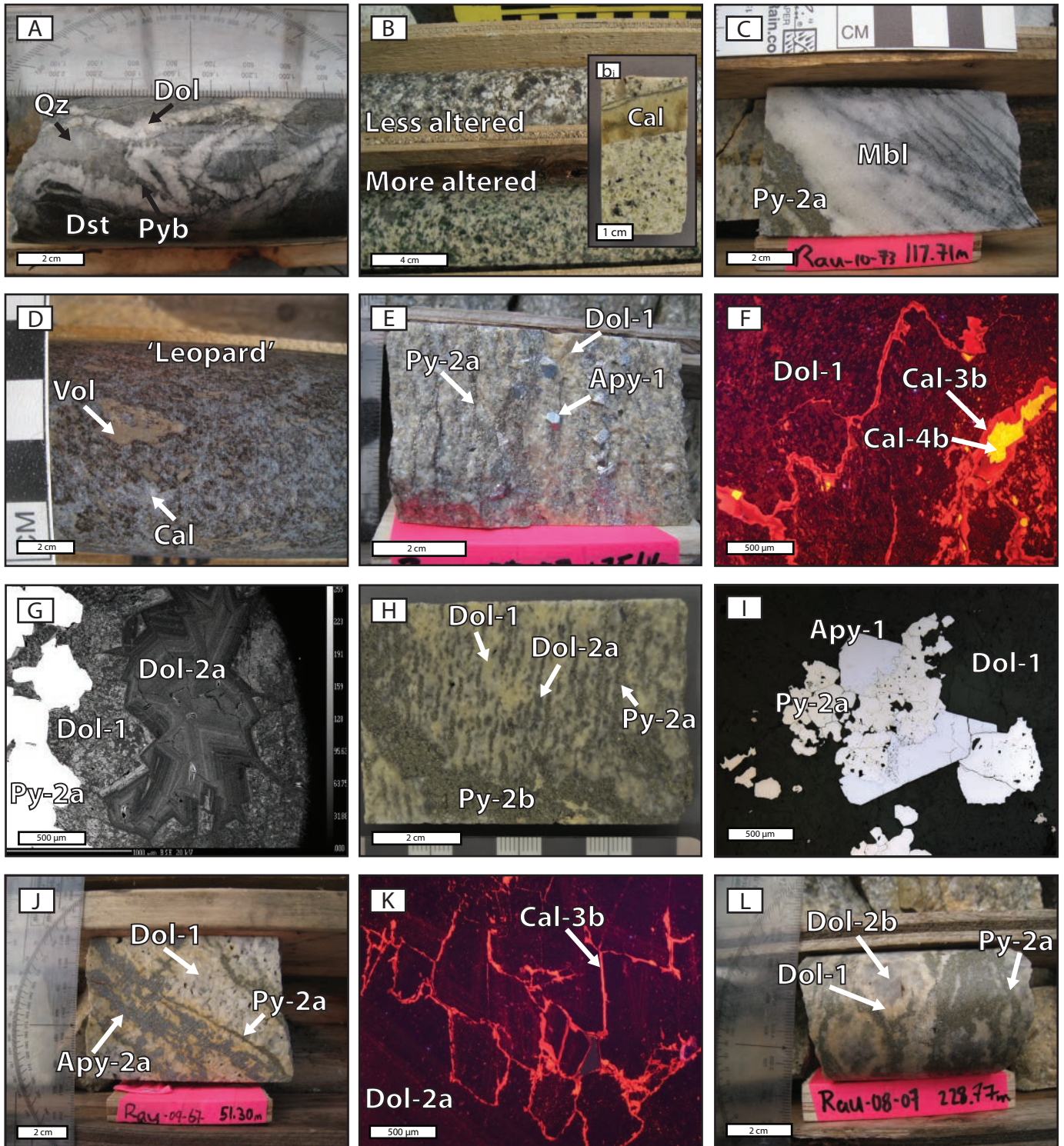
Fig. 7. Pictures and images of Tiger deposit, Rackla pluton rocks, and paragenetic relationships. A) Brecciated host-rock dolostone of the Bouvette Formation. B) Degrees of alteration within the Rackla pluton with inset image (bi) of crosscutting calcite vein. C) Tiger deposit marble crosscut by pyrite 2a. D) Calcite-rich volcanic rock of the "leopard" unit. E) Coeval dolomite 1 and arsenopyrite 1 crosscut by foliated pyrite 2a. F) CL image of dolomite 1 with two phases of calcite precipitating along grain boundaries. G) BSE image showing differing textures of dolomite 1 and dolomite 2a. H) Dolomite 1 crosscut by pyrite 2a and dolomite 2a, which are in turn overprinted by pyrite 2b. I) Dolomite 1 and arsenopyrite 1 are crosscut by pyrite 2a. J) Arsenopyrite 2a occurs parallel to pyrite 2a foliation, both of which overprint dolomite 1. K) CL image of banded dolomite 2a with calcite 3b precipitation along grain boundaries. L) Gray dolomite 2b occurring with dolomite 1 and pyrite 2a.

Table 1. Whole-Rock Major Element Oxide Data for the Rackla Pluton

| Sample ID		I074541	I074543	I074544	I074545	I074546	I074548	I074549	I074550	I074551	I074552	I074553	I074554	I074555
SiO_2	wt %	71.07	73.83	73.21	72.31	74.24	73.35	74.30	73.82	56.19	69.32	71.85	71.59	62.44
Al_2O_3	wt %	12.99	13.23	13.01	12.77	13.11	13.10	13.17	13.29	9.86	13.32	13.24	13.36	9.31
Fe_2O_3tot	wt %	1.42	1.52	1.48	2.01	1.33	1.85	1.67	1.95	13.92	4.43	2.32	1.69	12.11
FeO	wt %	1.23	1.29	1.16	1.67	1.16	1.55	1.41	1.54	12.05	n/a	1.68	1.28	8.61
CaO	wt %	2.30	1.74	1.74	1.14	1.63	1.73	1.82	1.65	1.02	0.82	1.25	2.21	0.66
MgO	wt %	0.58	0.24	0.23	0.21	0.20	0.21	0.24	0.23	0.71	0.52	0.36	0.31	0.98
Na_2O	wt %	2.32	2.37	1.61	0.60	2.39	2.21	2.85	2.56	0.19	0.13	0.38	0.22	0.15
K_2O	wt %	5.67	5.42	6.17	7.10	5.36	5.67	4.65	5.12	5.31	6.38	6.24	5.69	4.26
Cr_2O_3	wt %	<0.01	<0.01	<0.01	<0.01	<0.01	<0.01	0.01	<0.01	<0.01	<0.01	<0.01	<0.01	<0.01
TiO_2	wt %	0.20	0.21	0.20	0.15	0.16	0.19	0.19	0.21	0.13	0.17	0.19	0.19	0.12
MnO	wt %	0.04	0.04	0.09	0.21	0.05	0.06	0.02	0.06	1.78	0.44	0.14	0.11	1.19
P_2O_5	wt %	0.07	0.08	0.07	0.05	0.06	0.07	0.07	0.07	0.06	0.08	0.07	0.07	0.04
SrO	wt %	0.03	0.03	0.02	0.01	0.02	0.02	0.03	0.03	<0.01	0.01	0.01	<0.01	<0.01
BaO	wt %	0.07	0.06	0.07	0.07	0.06	0.07	0.05	0.06	0.05	0.05	0.06	0.05	0.02
LOI	wt %	1.85	1.20	2.09	2.59	1.22	1.41	0.77	0.88	9.39	3.97	3.39	4.25	6.81
Total	wt %	98.62	99.97	99.99	99.23	99.84	99.95	99.84	99.94	98.61	99.63	99.50	99.74	98.10
A/CNK		0.92	1.02	1.04	1.19	1.03	1.01	1.01	1.04	1.25	1.55	1.37	1.27	1.54
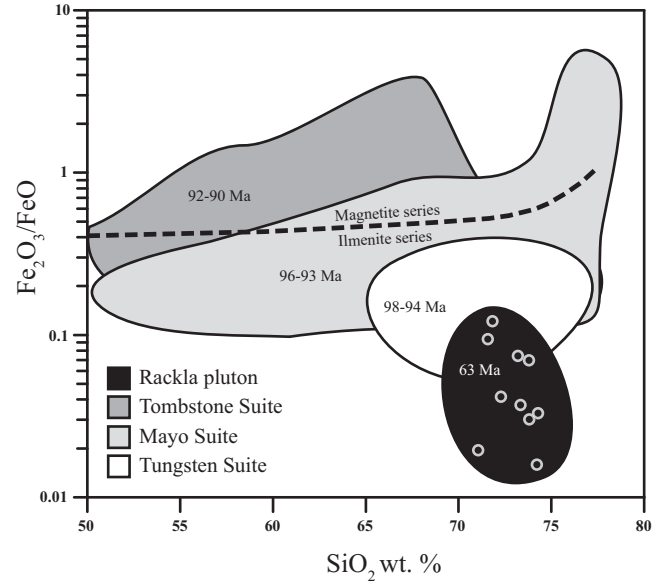
Fig. 8. Whole-rock ferric:ferrous ratios for nearby Cretaceous plutonic suites (Hart et al., 2004) and for the Rackla pluton. Dashed line separates magnetite and ilmenite series intrusions.

a "leopard" texture of alternating calcite and biotite (Fig. 7d). The volcanic nature of the unit is inferred from the presence of sub-cm lapilli fragments associated with secondary calcite in the weakly banded matrix of this unit. This basal unit also contains minor amounts of disseminated, euhedral magnetite at the contact with the basal volcanic package and overall appears to be strongly hydrothermally altered.

Tiger deposit mineralization: The following paragenetic descriptions are split into five mineralogically and texturally distinct stages, most with clear crosscutting relationships. Stages 1 and 2 consist of predominantly gold hosting dolomite-arsenopyrite-pyrite; stage 2 differs from stage 1 due to the presence of strain textures. Stages 3 and 4 crosscut stages 1 and 2 as discrete and massive overprinting pyrite-quartz-base metals and native gold. Stage 5 consists of calcite veining that crosscuts stages 1 to 4.

Stage 1: Dolomite 1 + gold-bearing arsenopyrite 1: Stage 1 of the paragenetic sequence involves the pervasive replacement of host-rock limestone/dolostone within the Discovery Horizon by dolomite 1 + arsenopyrite 1. This assemblage replaces the marble (Fig. 7c) or crosscuts it as rare, discrete, centimeter-scale veins. Dolomite 1 is the most volumetrically significant mineral in stages 1 and 2 and occurs as 2- to 4-mm, equant to elongate, pale pink to white crystals (Fig. 7e) that commonly exhibit saddle morphology as well as angular crystal boundaries and have triple-point grain textures. Both pink and white dolomite 1 have a mottled texture and luminesce dark red and black under cathodic light (Fig. 7f). This mottled texture is also visible in backscattered electron (BSE) images (Fig. 7g) as relatively brighter (Fe rich) and darker (Mg rich) shades of gray for both pink and white dolomite 1. The similar compositions, CL-active species, identical BSE response, and indistinguishable nature of the pink and white dolomite 1 phases under the microscope suggest a broadly coeval origin.

Euhedral arsenopyrite 1 is disseminated throughout dolomite 1 (Fig. 7e). Importantly, arsenopyrite 1 grains have angular crystal boundaries and no reaction rim with dolomite 1 and, thus, both these phases are in textural equilibrium and are considered to be coeval in the paragenetic sequence. Thin, <0.01-mm subparallel fractures are restricted to arsenopyrite 1 grains but are not observed to extend into the dolomite 1. Lattice-bound gold in arsenopyrite 1 was identified by dynamic secondary ion mass spectrometry (Stroshein et al., 2011).

Stage 2: (a) pyrite 2a + arsenopyrite 2a + dolomite 2a, (b) dolomite 2b + pyrite 2b: Stage 2a mineralization is characterized by an assemblage of fine-grained pyrite (pyrite 2a), coarse-grained arsenopyrite (arsenopyrite 2a), and dolomite (dolomite 2a) that have grown in parallel tabular arrays and define a prominent foliation (Fig. 7h). Pyrite 2a occurs as 0.1- to 0.5-mm equant, subhedral to cubic crystals that have both grown interstitially within dolomite 1 and overprint dolomite 1 and arsenopyrite 1 (Fig. 7i). Grain boundaries of pyrite 2a, dolomite 1, and arsenopyrite 1 are sharp, are inferred to be in textural equilibrium, and nondestructively overprint stage 1 mineralization. These pyrite 2a crystals have a weak elongate shape and commonly have triple-point textures. Backscattered electron imaging of pyrite 2a grains reveals that they are broadly homogeneous, although weak zoning is rarely observed and corresponds to varying As concentrations determined by energy dispersive spectrometry (EDS).

Arsenopyrite 2a consists of undeformed coarse-grained (0.5 cm) crystals that occur in tabular arrays parallel to pyrite 2a and within dolomite 1 (Fig. 7j). Although arsenopyrite 2a crosscuts dolomite 1, the euhedral nature of the crystals and lack of any reaction rim suggest arsenopyrite 2a is in textural equilibrium with dolomite 1. Aside from the tabular array of crystals, arsenopyrite 2a is identical to arsenopyrite 1; however, it is much less abundant than arsenopyrite 1.

Dolomite 2a forms 1-mm to 1-cm equant, blocky, light gray crystals (Fig. 7g, k) with angular crystal boundaries. The abundance of angular crystal faces, absence of both saddle morphology textures and sweeping extinction (under polarized light), and fewer fluid inclusions distinguish dolomite 2a from dolomite 1. Weak undulose extinction and bird's eye textures are much more common in dolomite 2a. Although no internal deformation or crystal elongation is observed besides some twinning, dolomite 2a occurs in elongate mineral clusters subparallel to pyrite 2a (Fig. 7g, h). Banding (Fig. 7g) is visible in BSE imaging where the darker zones are Mg rich and the lighter zones are richer in Fe. Dolomite 2a has a dark red to black luminescence (Fig. 7k) similar to dolomite 1 but is texturally elongate and, therefore, temporally distinct.

Stage 2b mineralization is characterized by an assemblage of fine-grained pyrite (pyrite 2b) and dolomite (dolomite 2b) that postdates or crosscuts the foliation. Pyrite 2b occurs as 0.1- to 0.5-mm, equant and subhedral crystals that form irregular crystal masses oblique to pyrite 2a (Fig. 7h). Pyrite 2b pervasively overprints stage 1 to 2a mineral assemblages with no preferred orientation.

Dolomite 2b forms 1-mm to 1-cm equant, blocky and light gray crystals with angular grain boundaries. The dolomite 2b appears almost identical to dolomite 2a, but does not have a preferred alignment parallel to the foliation and rather forms bulbous textures (Fig. 7l). Backscattered electron imaging of dolomite 2b reveals uniform growth zoning similar to that of dolomite 2a (e.g., Fig. 7g). EDS analysis indicates that darker zones in dolomite 2b have higher Mg concentrations and lighter zones correspond to higher relative Fe contents. Cathodoluminescence colors for zoned dolomite 2b range from dark red to black and are identical to the CL colors and textures of dolomite 2a. However, unlike pyrite 2b, dolomite 2b does not actively crosscut stage 1 or stage 2a minerals and, thus, its relationship with pyrite 2b remains unclear.

Stage 3: (a) pyrite 3a, (b) quartz 3b+ talc 3b + chlorite 3b + calcite 3b, (c) bismuthite 3c + gold 3c + bismuth 3c + pyrrhotite 3c + pyrite 3c: Stage 3a mineralization is characterized by coarse-grained (1 mm–>1 cm), brassy, euhedral to subhedral pyrite (pyrite 3a) that overprints stage 1 and 2 mineralization (Fig. 9a). Pyrite 3a is commonly associated with but predates quartz (quartz 3b).

Stage 3b mineralization comprises variable amounts of quartz 3b, talc 3b, chlorite 3b, and calcite 3b replacing and occurring in brittle fractures (Fig. 9b) crosscutting pyrite 3a and overprinting stage 1 and 2 mineral assemblages. Quartz 1 is the major constituent of stage 3b, generally occurring as anhedral accumulations (Fig. 9b) replacing stages 1 and 2 or, more rarely, as euhedral crystals. Chlorite occurs as small, 0.1- to 0.5-mm, radiating, acicular needles within quartz 3b (Fig. 9b). XRD analysis has identified talc in this stage; however, it has not been identified in thin section. The chlorite 3b and quartz 3b share sharp, angular grain boundaries and are considered to be coeval. Calcite 3b is characterized by centimeter-scale blocky and subhedral crystals occurring as a minor phase within quartz or as centimeter-scale veins crosscutting pyrite 3a. Calcite 3b also crosscuts dolomite 1, 2a, and 2b (Fig. 7f, k).

Stage 3c mineralization consists of bismuthinite (bismuthinite 3c), native gold (gold 3c), native bismuth (bismuth 3c), and pyrrhotite (pyrrhotite 3c) within fractures of stage 3b quartz 3b and pyrite 3a. Bismuthinite occurs as anhedral crystals within fractures of stage 1 and 2 sulfides, pyrite 3a, and quartz 3b (Fig. 9c, d) and has been observed in a few drill holes to occur in large centimeter-scale accumulations. Backscattered electron imaging has revealed rare bismuthinite rimming pyrite 3a crystals that are rimmed by a later anhedral pyrite 3c (Fig. 9c). Native gold occurs as rare anhedral fracture infill within stage 1 to 2 sulfide fractures and within pyrite 3a fractures. When native gold is present, it occurs adjacent to bismuthinite 3c in fractures and suggests coeval precipitation (Fig. 9e). Where observed, bismuth 3c is speckled within bismuthinite 3c as small <0.1-mm anhedral crystals. Similarly, pyrrhotite 3c commonly occurs within close proximity to bismuthinite 3c as anhedral masses with no apparent crosscutting relationship. However, bismuth 3c and pyrrhotite 3c are observed to crosscut bismuthinite 3c in fractures, suggesting a coeval to slightly late timing of pyrrhotite 3c to bismuthinite 3c + gold 3c mineralization.

Stage 4: (a) quartz 4a + sphalerite 4a + chalcopyrite 4a + dolomite 4a, (b) monazite 4b + actinolite 4b + scheelite 4b + muscovite 4b + calcite 4b + pyrite 4b: Stage 4a mineralization is characterized by fracture filling and replacement by quartz (quartz 4a), sphalerite (sphalerite 4a), chalcopyrite (chalcopyrite 4a), and dolomite (dolomite 4a). This mineral assemblage
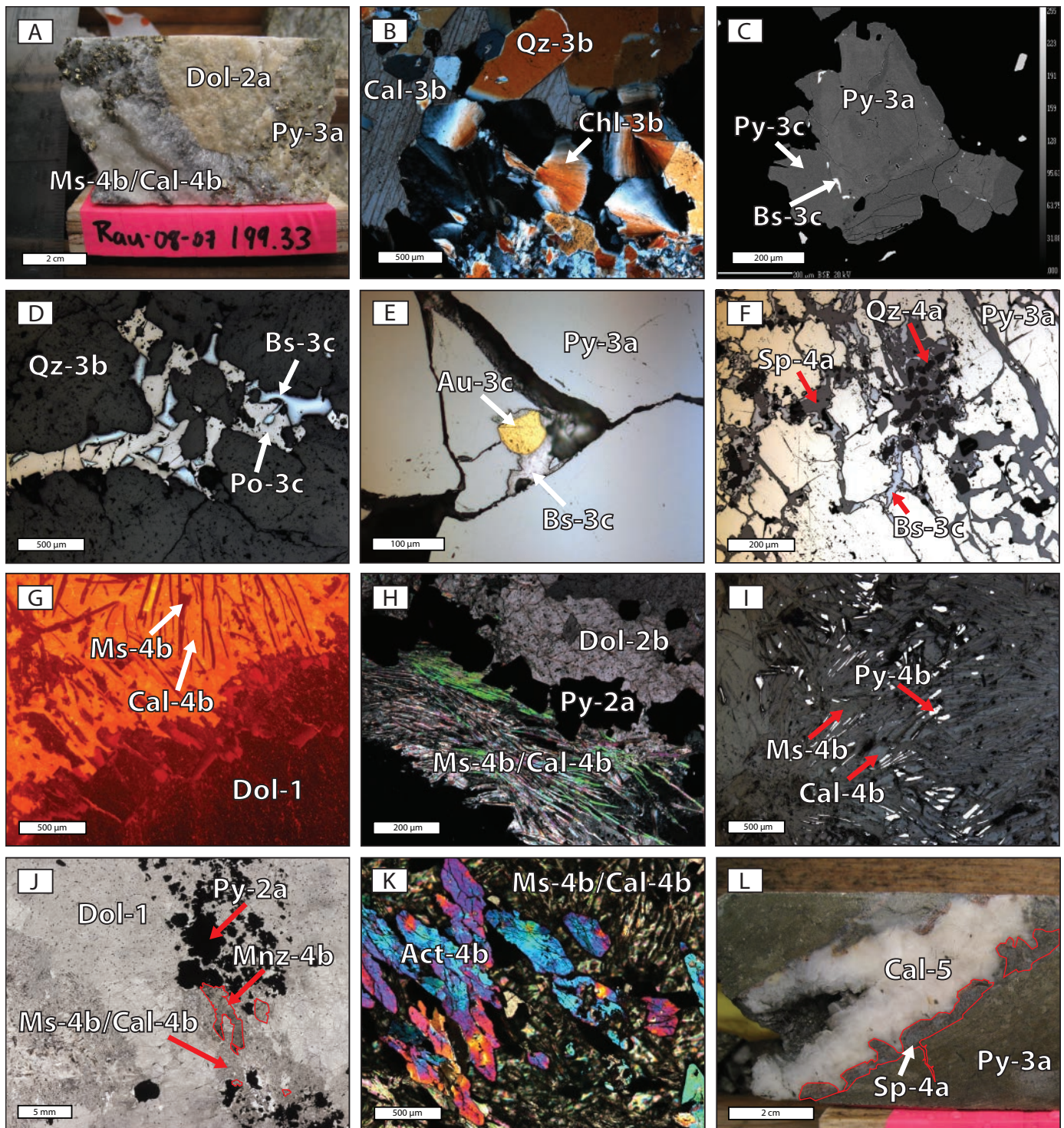
Fig. 9. A) Dolomite 1 is overprinted by coarse pyrite 3a and later muscovite 4b and calcite 4b. B) Quartz 3b, calcite 3b, and radiating chlorite 3b occur as a phase cutting pyrite 3a. C) BSE image showing two phases of pyrite growth, pyrite 3a and pyrite 3c, separated by an intermediate phase of bismuthinite 3c mineralization. D) Bismuthinite 3c and pyrrhotite 3c occupying fractures in quartz 3b. E). Gold 3c and bismuthinite 3c occur associated in pyrite 3a fractures. F) Pyrite 3a is fractured and filled by bismuthinite 3c, sphalerite 4a, and quartz 4a mineralization. G) CL image of muscovite 4b and calcite 4b overprinting dolomite 1. H) Muscovite 4b and calcite 4b exploiting rheologic contrasts at mineral phase boundaries. I) Pyrite 4b occurring within muscovite and calcite 4b mineralization. J) Plane-polarized light image of monazites (outlined in red) crosscut by muscovite 4b and calcite 4b assemblage. K) Actinolite is crosscut by muscovite 4b and calcite 4b assemblage. L) Sphalerite 4a (outlined in red) rims a vein in pyrite 3a that is filled by later calcite 5 mineralization.

is commonly observed infilling bismuthinite-bismuth veinlets within pyrite 3a (Fig. 9f). Euhedral quartz 4a and minor anhedral sphalerite 4a occur in fractures in pyrite 3a (Fig. 9f) and are associated with rare anhedral crystals of chalcopyrite 4a occurring within fractures of sphalerite 4a, suggesting chalcopyrite 4a is coeval to slightly epigenetic to the sphalerite 4a. Sphalerite 4a is also observed lining large centimeter-scale calcite 5 veins as euhedral zoned crystals (Fig. 9l). Associated with stage 4a is a euhedral to anhedral dolomite (dolomite 4a) that commonly occurs with euhedral sphalerite 4a and is observed to crosscut and offset fractures filled with sphalerite 4a.

Stage 4b mineralization consists of monazite (monazite 4b), actinolite (actinolite 4b), scheelite (scheelite 4b), muscovite (muscovite 4b), calcite (calcite 4b), and pyrite (pyrite 4b). The main constituents of this phase are calcite 4b and muscovite 4b. Calcite 4b occurs as subhedral crystals that range from 0.01 mm to 1 cm in diameter and are intergrown with muscovite 4b (Fig. 9g-i). Muscovite 4b forms both parallel, acicular crystals 0.5 mm long (Fig. 9g) and irregular radiating aggregates. Muscovite 4b and calcite 4b commonly form along rheologic boundaries, such as between dolomite 1 or 2 and sulfides (Fig. 9h). Pyrite 4b is a minor constituent of this phase and occurs interstitial to the muscovite 4b and calcite 4b as small 0.01-mm anhedral crystals (Fig. 9i). Crosscutting relationships of pyrite 3c and pyrite 4b are not observed and, therefore, their relationship is unknown. Stage 4b mineral phases destructively overprint stage 1 to 3a mineral assemblages. Calcite 4b has bright red and orange luminescence under cathodic light (Fig. 9g) and is very distinct from calcite 3b and stage 1 to 2 dolomites. Calcite 4b also occurs along grain boundaries of dolomite 1, 2a, and 2b and appears to infill void space postdating calcite 3b, determined by CL (Fig. 7f). Monazite 4b, actinolite 4b, and scheelite 4b are all present within stage 4b yet are not observed in contact with one another; thus, the relative crosscutting relationships are unclear. Monazite 4b is observed to form only within muscovite 4b/calcite 4b aggregates and occurs as large 0.5- to 2-mm euhedral crystals (Fig. 9j). Small fractures in monazite 4b grains are occupied by muscovite 4b or calcite 4b crystals and locally small thorite grains, suggesting monazite predates these minerals. Actinolite 4b is associated with the muscovite 4b/calcite 4b assemblage in dense mineral clusters (Fig. 9k). No obvious temporal relationship is observed between actinolite 4b grains, suggesting coeval growth with the muscovite 4b/calcite 4b assemblage. Scheelite 4b is a rare component and occurs as 1-cm-diameter subhedral crystals that have fractures infilled with muscovite 4b and calcite 4b. Stage 4b minerals were not found in association with stage 4a minerals; thus, the two stages may be coeval.

Stage 5: Calcite 5: Calcite 5 is found in the center of centimeter-scale brittle fractures that crosscut stages 1 to 4 (Fig. 9l). Calcite 5 is coarse grained with crystals often up to 1 cm in diameter.

Microthermometry

Microthermometric analyses were performed on fluid inclusion assemblages (FIAs, Goldstein and Reynolds, 1994) in dolomite 1, dolomite 2b, quartz 3b, sphalerite 4a, and from Rackla pluton magmatic quartz and crosscutting veins, thus spanning most of the paragenetic sequence. Based on the criteria of Roedder (1984), fluid inclusions were categorized as primary, pseudosecondary, or secondary and also categorized by their room-temperature phase assemblage. Since none of the mineral phases had discernable growth zones (excluding sphalerite 4a), a primary origin was assigned to inclusions in minerals with a consistent CL signature and that occurred in random orientations in the wafer. Inclusions that appeared necked and had very irregular shapes were not analyzed due to potential postentrapment modification. Below, FIAs are described with respect to their paragenesis (Figs. 10, 11) and data are presented as averages (Table 2).

Rackla pluton: Fluid inclusions were found in single quartz crystals in the granitoid rock, but were very rare and were smaller than 15 μm (Fig. 10a). One primary FIA consisting of liquid water + carbonic liquid inclusions was analyzed. Salinities calculated from melting temperature (T_M) have an average of 15 wt % NaCl equiv; however, clathrate should have formed but was not observed. Thus, these salinities are overestimated. Some inclusions had total homogenization temperatures of 341°C, but some inclusions decrepitated at higher temperatures (T_D; 370°C). Primary aqueous (liquid water + water vapor) FIAs also occurred in quartz and had a salinity of 12 wt % NaCl equiv and an average homogenization temperature (T_H) of 227°C (Table 2). Halite-saturated primary aqueous FIAs (liquid water + water vapor + solid halite) are rare and their calculated salinity is approximately 29 wt % NaCl equiv. Secondary trails that crosscut the quartz grains and contain liquid water + water vapor inclusions were common. These FIAs have a calculated salinity of 15 wt % NaCl equiv and a T_H average of 259°C. Late calcite veins crosscut the Rackla pluton (Fig. 7b) and contain rare primary fluid liquid water + water vapor inclusions (Fig. 10b) with calculated salinities of ca. 16 wt % NaCl equiv and T_H of 290°C.

Tiger deposit dolomite 1: Dolomite 1 contains abundant fluid inclusions. Many of the inclusions appeared to be primary but are small (<10 μm) and, due to the optics of the dolomite, it was difficult to observe phase transitions. Primary FIAs consisting of carbonic liquid + liquid water, liquid water + carbonic liquid + solid halite + solid opaque, and liquid water + carbonic liquid were observed within dolomite 1. Aqueous carbonic inclusions (carbonic liquid + liquid water) are the most abundant inclusion (Fig. 10c). These inclusions had dark rims (refraction effect) on their perimeter, making the thin liquid water portion very difficult to see, and, thus, microthermometric data from these inclusions are rare. During the heating run, melting temperatures of CO_2 were mostly within error of –56.6°C with some values of –57.2°C, which may indicate the presence of another volatile phase such as CH_4 or N_2 (Roedder, 1984). Aqueous T_M was not observable and the T_H averaged at ca. 300°C. A less abundant, liquid water + carbonic liquid + solid halite + solid opaque inclusion type was observed in the same FIA with carbonic liquid + liquid water and liquid water + carbonic liquid inclusions. In these halite-bearing inclusions (Fig. 10d), the solid opaque occurred as a very small black speck attached to halite cubes, but was not always visible in all inclusions. Halite dissolution temperatures resulted in calculated salinities of 31 to 45 wt % NaCl equiv. The inclusions decrepitated before they homogenized with an average T_D of 317°C. Rare liquid water + carbonic
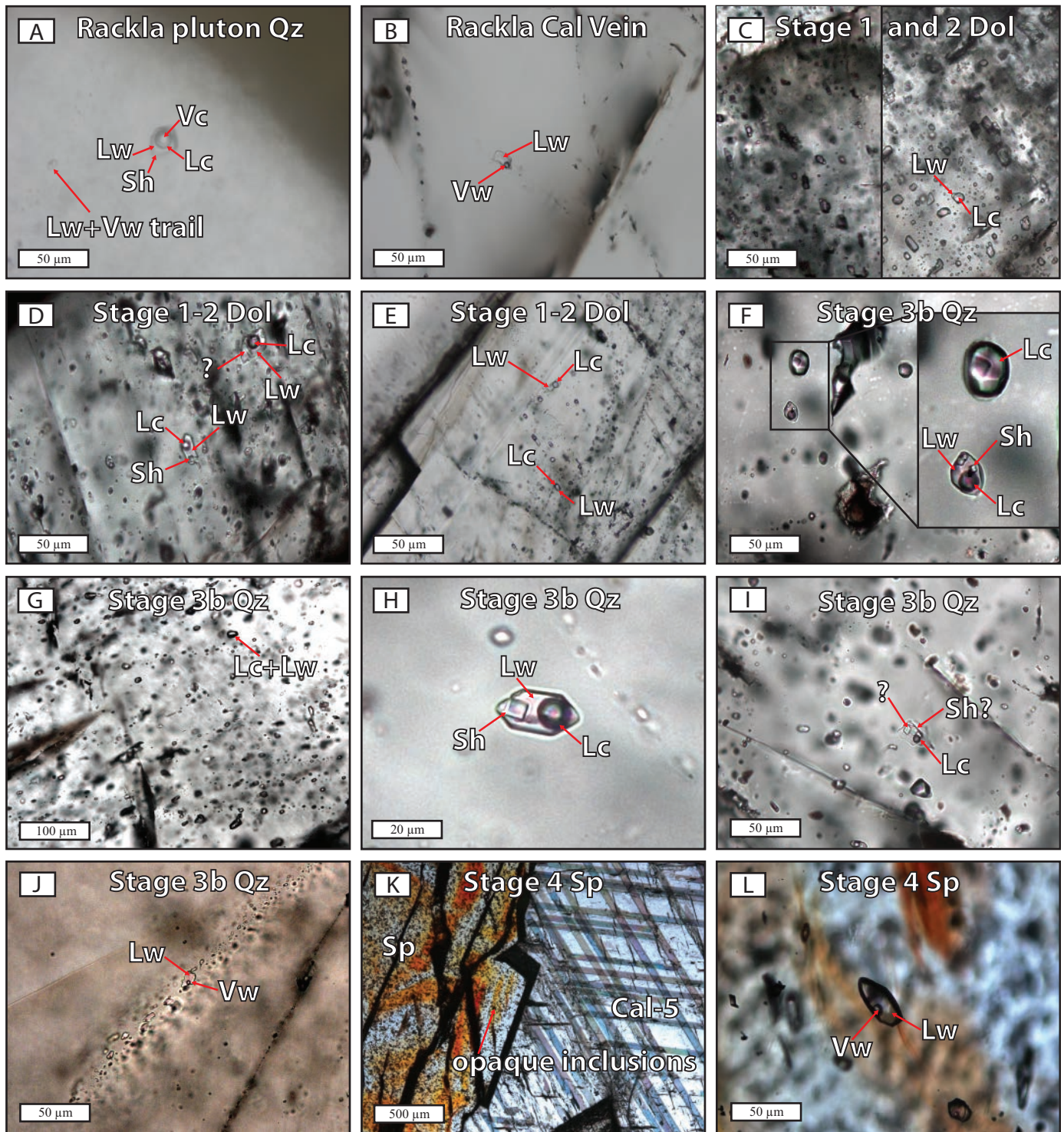
Fig. 10. Images of fluid inclusions hosted in the Rackla pluton and the Tiger deposit. A) Aqueous-carbonic inclusions in magmatic quartz are cut by trail-hosted aqueous inclusions. B) Primary aqueous inclusions in a calcite vein cutting the Rackla pluton. C) Abundant carbonic inclusions in stage 1 and 2 dolomite. D) Aqueous-carbonic brine and multisolid inclusions within stage 1 and 2 dolomite. E) Aqueous-carbonic inclusions of varying proportions occurring within stage 1 and 2 dolomite. F) Unmixing assemblage of carbonic and aqueous-carbonic brine inclusions in quartz 3b. G) Abundant carbonic inclusions within quartz 3b. H) Typical relative phase proportions within a carbonic-brine inclusion in quartz 3b. I) Irregularly shaped multisolid inclusions adjacent to carbonic inclusions in quartz 3b. J) Trail-hosted aqueous inclusions cutting quartz 3b. K) Relationship of calcite 5 to earlier sphalerite 4a. L) Trail-hosted aqueous inclusion within sphalerite 4a thought to be sourced from calcite 5-forming fluid.
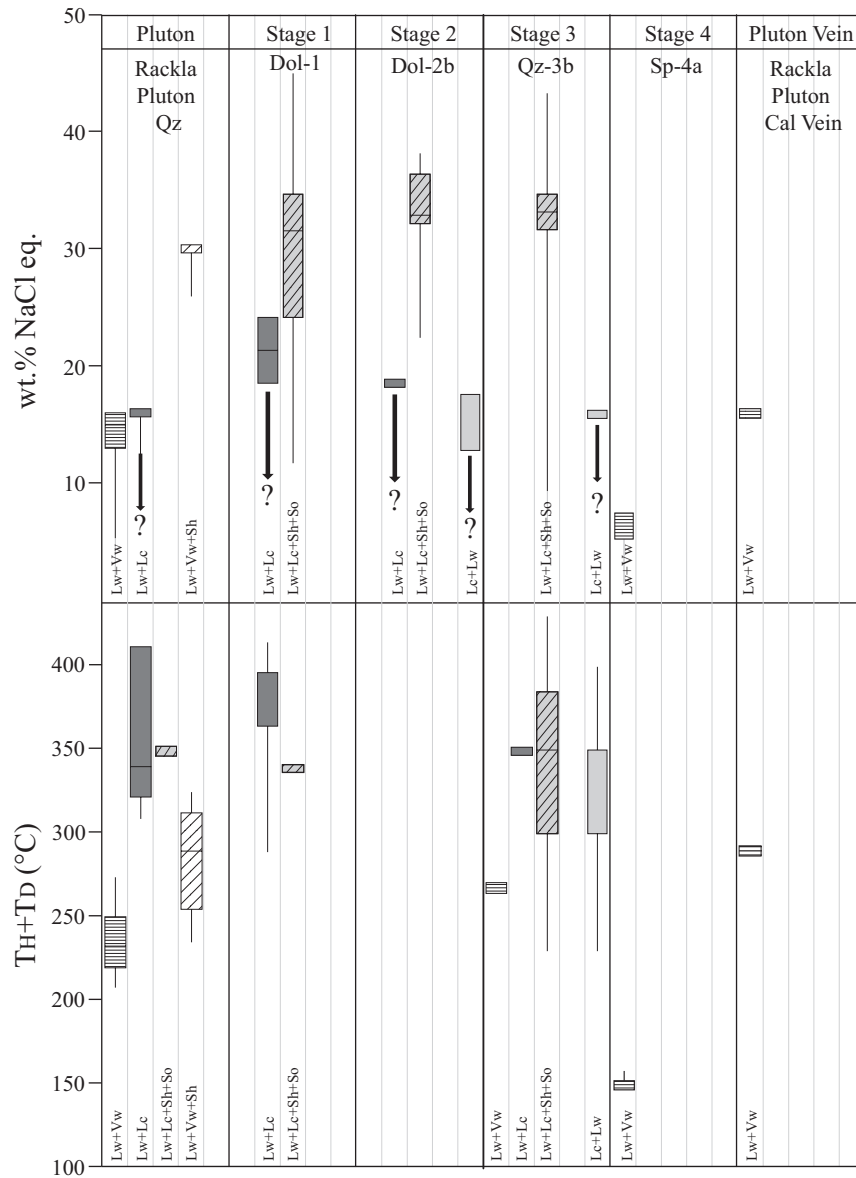
Fig. 11. Salinity and temperature data from fluid inclusions with respect to paragenesis. Arrows illustrate potential real compositions of carbonic inclusions where clathrate data was not obtained. Temperatures of decrepitation and homogenization are used together because values are similar for individual FIAs and because few T_H were observed. The distributions of T_H and T_D data are found in Table 2.

liquid (Fig. 10e) inclusions also occur with salinity values of 9 to 24 wt % NaCl equiv, yet no clathrate was observed and reported salinities are overestimated. The homogenization temperatures in these inclusions have an average of 406°C, and decrepitation temperatures had a range between 290° and 365°C. Secondary trails of <2-μm liquid water + water vapor inclusions crosscut dolomite 1 primary FIA; however, the small size of the inclusions within the trails did not allow for microthermometric measurements.

Tiger deposit dolomite 2b: The FIAs in dolomite 2b are very similar to FIAs in dolomite 1 in that they contain primary carbonic liquid + liquid water, liquid water + carbonic liquid + solid halite + solid opaque, and rare liquid water + carbonic liquid fluid inclusions, all of which have microthermometric properties similar to dolomite 1 (Table 2). This primary FIA is

also crosscut by secondary liquid water + water vapor trails that were too small to make microthermometric measurements.

Tiger deposit quartz 3b: Fluid inclusion assemblages in quartz 3b (Fig. 10f) are comparable to the FIAs hosted in dolomite 1 and dolomite 2b and have similar microthermometric properties. Primary FIAs of carbonic liquid + liquid water, liquid water + carbonic liquid + solid halite + solid opaque, and liquid water + carbonic liquid occur within quartz 3b. Liquid water + carbonic liquid + solid halite + solid opaque inclusions (Fig. 10f-i) are subordinate to and coeval with carbonic liquid + liquid water inclusions and resemble the inclusion in Figure 10h, with negative crystal shapes. Secondary trails of liquid water + water vapor inclusions occurred crosscutting primary phases in quartz 3b (Fig. 10j) and were generally too small (<10 μm) to observe accurate phase transitions.

Table 2. Summary of Microthermometric Data

n	FIA	Phase	Type	P, PS, S	T_{MCO_2} Min	Max	Avg	T_{HCO_2} Min	Max	Avg	T_{FM}	T_M	$T_{M\,halite}$	NaCl (wt %)	T_D	T_H	Liquid	Vapor	Solid
8	33	RP-Qz	Lw + Vw + Sh	P							−33		152	29		284	0.85	0.10	0.05
11	35	RP-Qz	Lw + Vw	P							−22	−8		12		227	0.95	0.05	0.00
1	34	RP-Qz	Lw + Lc + Sh	P			−56.7			26	−22		>350	>40	350		0.85	0.10	0.05
11	36	RP-Qz	Lw + Lc	P			−56.6			28	−28	−11		15	370	341	0.90	0.10	0.00
7	33	RP-Qz	Lw + Vw	S							−30	−11		15		259	0.95	0.05	0.00
5	32	RP-Cal	Lw + Vw	P							−28	−12		16		290	0.95	0.05	0.00
10	1	Dol-1	Lw + Lc	P	−56.6	−56.2	−56.4	28	29	29	−39					406	0.56	0.44	0.00
1	1	Dol-1	Lw + Lc + Sh	P			−56.3			28			380	45	365		0.50	0.49	0.01
6	19	Dol-1	Lc + Lw	P	−56.8	−56.6	−56.7	15	22	17	−35	−23		24			0.32	0.68	0.00
2	19	Dol-1	Lw + Lc	P	−56.6	−56.3	−56.5	20	28	24	−35	−23		24			0.55	0.45	0.00
9	19	Dol-1	Lw + Lc + Sh	P	−65.0	−56.4	−57.9	24	28	27	−30	−8		12			0.66	0.29	0.05
3	19	Dol-1	Lw + Lc + Sh + So	P	−65.0	−56.4	−59.8	22	30	26							0.78	0.17	0.05
3	20	Dol-1	Lw + Lc	P			−57.0				−35	−22		24			0.70	0.30	0.00
13	20	Dol-1	Lw + Lc + Sh	P	−60.0	−57.0	−59.0					−22					0.67	0.28	0.05
6	21	Dol-1	Lw + Lc	P							−33	−22	171	31	290		0.70	0.30	0.00
1	21	Dol-1	Lw + Lc + Sh	P											340		0.63	0.28	0.08
3	22	Dol-1	Lc + Lw	P			−56.4			23	−36						0.20	0.80	0.00
6	22	Dol-1	Lw + Lc	P			−56.4			30	−35		226	33			0.90	0.10	0.00
2	22	Dol-1	Lw + Lc + Sh	P			−56.4			30	−38		250	35			0.66	0.25	0.06
9	23	Dol-1	Lw + Lc	P	−57.4	−56.6	−56.4	28	30	29		−15		9			0.65	0.30	0.05
7	23	Dol-1	Lw + Lc + Sh	P			−56.4			29							0.73	0.27	0.05
6	30	Dol-1	Lc + Lw	P			−57.2	10	15	13	−35						0.69	0.23	0.09
11	31	Dol-1	Lc + Lw	P	−56.7	−56.6	−56.6	17	22	20			213	33			0.20	0.80	0.00
4	31	Dol-1	Lw + Lc	P	−56.7	−56.6	−56.6	18	19	26							0.70	0.30	0.00
2	31	Dol-1	Lw + Lc + Sh + So	P	−56.6		−56.6				−33						0.85	0.10	0.05
9	24	Dol-2b	Lc + Lw	P	−56.9	−56.5	−56.6	4	17	10	−36						0.11	0.89	0.00
1	24	Dol-2b	Lw + Lc + Sh	P			−56.6			27	−35	−15		19			0.69	0.30	0.01
14	25	Dol-2b	Lc + Lw	P	−56.6	−56.4	−56.6	10	26	18	−23	−11		14			0.26	0.74	0.00
3	25	Dol-2b	Lw + Lc + Sh	P			−56.6	23	29	25	−35		283	37			0.75	0.20	0.05
11	26	Dol-2b	Lc + Lw	P	−57.0	−56.6	−56.6	3	16	12							0.20	0.80	0.00
4	26	Dol-2b	Lw + Lc	P			−56.6	12	27	21	−35	−15		19			0.70	0.30	0.00
5	26	Dol-2b	Lw + Lc + Sh	P			−56.6	22	27	24	−35	−20	212	30			0.60	0.30	0.10
1	2	Qz-3b	Lw + Vw	Unk			−60.0			3	−35					268	0.95	0.05	0.00
3	3	Qz-3b	Lw + Lc + Sh	P			−57.7			25	−10		163	30	230		0.50	0.45	0.05
2	4	Qz-3b	Lc + Lw	P			−57.0	23	25	24	−11					350	0.20	0.80	0.00
2	4	Qz-3b	Lw + Lc	P	−57.8	−56.8	−57.4			22	−23					278	0.80	0.20	0.00
3	4	Qz-3b	Lw + Lc + Sh	P			−56.8	17	20	19	−26				400		0.83	0.16	0.01
5	4	Qz-3b	Lw + Lc + Sh + So	P			−57.1	12	14	12						410	0.73	0.26	0.01
11	5	Qz-3b	Lc + Lw	P	−57.1	−56.8	−56.8	10	19	15	−25				300		0.20	0.80	0.00
9	6	Qz-3b	Lc + Lw	P			−56.4			28	−30		355	43	300		0.20	0.80	0.05
2	6	Qz-3b	Lw + Lc + Sh + So	P													0.65	0.30	0.05
3	7	Qz-3b	Lc + Lw	P	−61.6	−61.1	−61.3	2	6	3	−30				360		0.20	0.20	0.00
2	7	Qz-3b	Lw + Lc + Sh	P	−63.0	−61.5	−62.3			2	−25		154	30	343		0.70	0.20	0.10
21	8	Qz-3b	Lc + Lw	PS	−57.6	−57.4	−57.6	13	20	17	−20	−12		16	356		0.20	0.80	0.00
44	9	Qz-3b	Lc + Lw	P	−57.2	−56.6	−56.8	7	15	10							0.20	0.80	0.00
9	10	Qz-3b	Lc + Lw	P			−57.2	6	7	7	−32						0.78	0.22	0.00
3	10	Qz-3b	Lw + Lc	P			−57.0	9	20	14	−26						0.94	0.05	0.01
2	10	Qz-3b	Lw + Lc + Sh + So	P			−58.2			17	−30	−3					0.19	0.80	0.01
1	11	Qz-3b	Lc + Lw	PS			−61.2			−1							0.20	0.80	0.00

Table 2. *(Cont.)*

n	FIA	Phase	Type	P, PS, S	T_{MCO_2} Min	Max	Avg	T_{HCO_2} Min	Max	Avg	T_{FM}	T_M	$T_{Mhalite}$	NaCl (wt %)	T_D	T_H	Liquid	Vapor	Solid
22	11	Qz-3b	Lw + Lc + Sh	PS	−68.0		−58.5	3	12	9	−35		165	30			0.80	0.18	0.02
11	12	Qz-3b	Lc + Lw	P	−57.0	−56.6	−56.8	8	27	23	−20				300		0.51	0.49	0.00
1	12	Qz-3b	Lw + Lc + nS	P							−35		210	32		200	0.80	0.10	0.10
5	12	Qz-3b	Lw + Lc + Sh	P							−37	−19	226	31	300	277	0.70	0.18	0.12
8	12	Qz-3b	Lw + Lc + Sh + So	P							−36	−20	206	29	300		0.69	0.23	0.09
17	13	Qz-3b	Lc + Lw	P	−56.8	−56.2	−56.7	17	24	20							0.24	0.76	0.00
1	13	Qz-3b	Lc + Lw + Sh	P			−56.6			27							0.65	0.30	0.05
4	13	Qz-3b	Lw + Lc	P	−56.8	−56.6	−56.7	27	29	28							0.70	0.30	0.00
4	13	Qz-3b	Lw + Lc + Sh	P	−56.8	−56.2	−56.4	16	28	22	−32						0.83	0.12	0.05
5	14	Qz-3b	Lc + Lw	P	−57.4	−56.7	−57.2	20	24	22	−35	−24	241	34		250	0.26	0.74	0.00
14	14	Qz-3b	Lw + Lc + Sh	P	−57.4	−56.6	−57.0	23	25	24	−30	−21	239	33			0.76	0.15	0.09
10	14	Qz-3b	Lw + Lc + Sh + So	P			−56.6			25							0.78	0.16	0.06
1	15	Qz-3b	Lw + Vw + nS	Unk							−25	−7	209	32	209				
3	16	Qz-3b	Lc + Lw	PS				10	13	12							0.20	0.80	0.00
7	16	Qz-3b	Lw + Lc + Sh	P			−56.4	17	21	19	−36						0.62	0.23	0.15
4	17	Qz-3b	Lw + Vw + nS	Unk							24	28		27			0.75	0.05	0.20
11	18	Qz-3b	Lc + Lw	P	−57.7	−56.9	−57.3	12	20	15					350		0.30	0.70	0.00
1	18	Qz-3b	Lw + Lc	P			−56.6			17					350		0.50	0.50	0.00
8	18	Qz-3b	Lw + Lc + Sh + So	P	−57.1	−56.4	−56.6	11	22	18	−32	−15	237	34	359		0.71	0.24	0.05
20	27	Sp-4a	Lw + Vw	S							−13	−4		7		151	0.02	0.98	0.00
1	28	Sp-4a	Lw + Vw	S								−1		1		153	0.02	0.98	0.00
10	29	Sp-4a	Lw + Vw	S							−10	−3		5		150	0.02	0.98	0.00

Notes: Shaded rows correspond to FIAs and all measurements are recorded in °C; total number (n) of inclusions measured are listed for FIAs and inclusion types; however, some individual inclusions do not have all microthermometric data recorded and, thus, data in this table do not correspond to the exact number of listed measured inclusions

Abbreviations are as follows: Cal = calcite, Dol = dolomite, Int = intrusion, Lc = carbonic liquid, LVS = volumetric proportions of liquid, vapor, and solid, Lw = liquid water, nS = multiple solids, P = primary, PS = pseudosecondary, Qz = quartz, RP = Rackla pluton, S = secondary, Sh = solid halite, So = solid opaque, Sp = sphalerite, T_D = decrepitation temperature, T_{FM} = temperature of first aqueous ice melting, T_H = total homogenization temperature, T_{HCO_2} = homogenization temperature of the CO_2 phase, T_M = final melting of aqueous ice, T_{MCO_2} = final ice melting of CO_2, $T_{Mhalite}$ = dissolution temperature of halite, Vc = carbonic vapor, Vw = water vapor

Tiger deposit sphalerite 4a: Sphalerite 4a contains abundant growth zones and fluid inclusions; however, most of these inclusions appeared opaque (Fig. 10k). Secondary liquid water + water vapor fluid inclusions were present (Fig. 10l), were 10 to 30 μm long, and occurred in planar trails cutting across growth zones. Calculated salinities were 1 to 7 wt % NaCl equiv and homogenization temperatures (T_H) had a range from 150° to 153°C.

Carbon, oxygen, sulfur and strontium isotopes

Carbon, oxygen, sulfur, and strontium isotopes were analyzed to assess a potential link between host rocks, gold-bearing mineralization, and the Rackla pluton. Carbonate and quartz samples were collected throughout the mineralized horizon in order to obtain a representative geochemical signature of the entire deposit. These results are tied to the paragenesis of the Tiger deposit and the fluid inclusions in order to better constrain the origin of mineralizing fluids, source of metals, and mechanisms of deposition. Carbon and oxygen isotope data are presented in Table 3 and Figure 12, sulfur isotope data are found in Table 4 and Figure 13, and strontium isotope data are presented in Table 5 and Figure 14.

Discussion

Isotopic characteristics of the host-rock carbonates and volcanic rocks

Unaltered Ordovician to Silurian marine carbonates have $\delta^{13}C$ values of –2 to 3‰ and $\delta^{18}O$ values of 20 to 23‰ (Veizer et al., 1999). The Ordovician to Silurian Bouvette Formation limestones have $\delta^{13}C$ values that range from –3.8 to 3.2‰ and $\delta^{18}O$ values that range from 16.2 to 22.3‰ and are positively correlated (Fig. 12). Some limestones have a higher $\delta^{13}C$ value of 3.2‰, $\delta^{18}O$ value of 22.3‰, and low values of $^{87}Sr/^{86}Sr$ at 0.70858, and are within the range of Ordovician to Silurian normal marine carbonates. However, overall, a trend of decreasing $\delta^{13}C$ and $\delta^{18}O$ values away from the marine carbonate compositions occurs and corresponds with increasing $^{87}Sr/^{86}Sr$ values up to 0.72642 (Fig. 14). This trend toward lower $\delta^{18}O$ and $\delta^{13}C$ values and more elevated $^{87}Sr/^{86}Sr$ values suggests that the limestone host rocks and an unidentified source of high $^{87}Sr/^{86}Sr$ values define two isotopically distinct reservoirs, and the altered limestone host rocks have compositions generated by mixing between these two end-members (discussed below).

Nature of the Rackla pluton and marble development

The Rackla pluton is one of two known intrusive occurrences (Fig. 2) within ~3 km of the Tiger deposit consisting of weakly peraluminous (Table 1), highly fractionated granitoids with local zones of pegmatite. A zone of tungsten-bearing hornfels that occurs proximal to the Rackla pluton and about 2 km from the Tiger deposit is associated with aplitic and pegmatitic dikes and sills that have $^{40}Ar/^{39}Ar$ muscovite ages of 62.3 ± 0.7, 62.4 ± 1.8, and 59.1 ± 2.0 Ma (Kingston et al., 2010). Kingston et al. (2010) analyzed the Pb isotope composition of feldspars in these dikes and found high values of $^{206}Pb/^{204}Pb$ from 19.768 to 19.945 and $^{207}Pb/^{204}Pb$ from 15.676 to 15.767. These values are distinctly different from those of the Tombstone and McQuesten suite feldspars, which have $^{206}Pb/^{204}Pb$
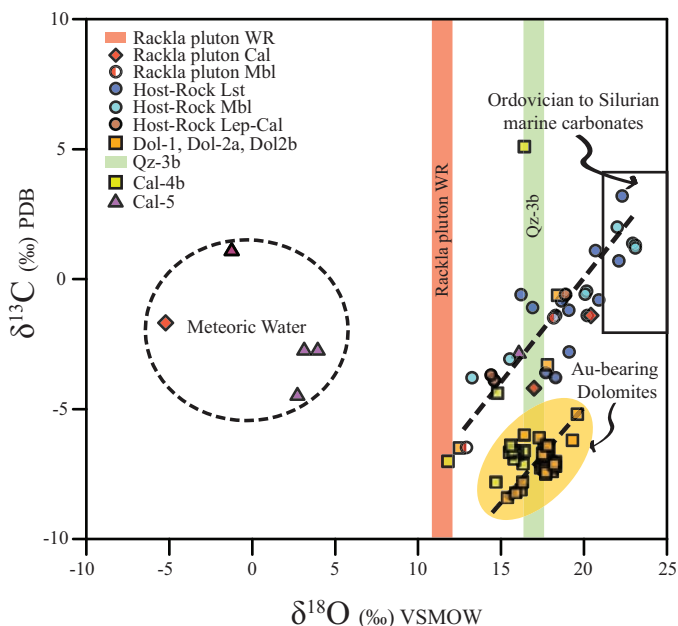

Fig. 12. Plot of $\delta^{13}C$ vs. $\delta^{18}O$ of Tiger deposit host rocks, hydrothermal mineralization, and Rackla pluton rocks. Rackla pluton whole-rock and quartz 3b samples have no associated $\delta^{13}C$ values and are thus represented graphically as solid bars. The Ordovician to Silurian marine carbonate box is derived from Veizer et al. (1999), and meteoric waters are represented by values below and near 0‰ $\delta^{18}O$. Two distinct isotopic trends occur for the host rocks and marbles and the gold-hosting dolomite, respectively.

values that range from 19.00 to 19.40 and $^{207}Pb/^{204}Pb$ values that range from 15.65 to 15.70 (Kingston et al., 2010). The Paleocene age, as determined by Ar-Ar age dates of Kingston et al. (2010), and Pb isotope signature of the Rackla pluton suggest it is distinct from the well-known mid- to Late Cretaceous Tombstone-Tungsten magmatic belt intrusions.

The whole-rock Rackla pluton samples have $\delta^{18}O$ values of 11.2 and 11.7‰, which are comparable to Tombstone-Tungsten magmatic belt values. Sulfur isotope values of disseminated magmatic sphalerite and arsenopyrite within the Rackla pluton range from 6.0 to 6.6‰ and contrast with the intrusions of the Tombstone plutonic suite, which typically have negative $\delta^{34}S$ values (Marsh et al., 2003; Mair et al., 2006a) due to their incorporation of biogenic sulfide from the metasedimentary rocks of the Selwyn Basin (e.g., Boyle et al., 1970). The positive $\delta^{34}S$ values of the Rackla pluton may be due to the assimilation of units with high $\delta^{34}S$ values, such as locally occurring sulfate (M. Dumala, pers. commun., 2010).

Numerous plutonic suites in the northern Cordillera, including the Tombstone-Tungsten magmatic belt, have been classified based on their age, spatial distribution, redox state, peraluminosity, magnetic susceptibility, and associated metallogenic signature (Hart et al., 2004). Magnetite and ilmenite series or oxidized and reduced classifications are based on the work of Ishihara (1977) and subsequent development of the concept (e.g., Ishihara et al., 2000; Ishihara, 2004). The Tombstone-Tungsten magmatic belt intrusions generally exhibit highly radiogenic strontium (0.710–0.730), high $\delta^{18}O$ values (11–13), low magnetic susceptibility (<3 × 10-3 SI

Table 3. All δ^{13}C and δ^{18}O Values for Analyzed Samples Including Sample ID, Mineralogy, and Paragenetic Stage

Sample ID	Phase	Stage	δ^{13}C$_{PDB}$ (‰)	δ^{18}O$_{V-SMOW}$ (‰)	Sample ID	Phase	Stage	δ^{13}C$_{PDB}$ (‰)	δ^{18}O$_{V-SMOW}$ (‰)
08-07 61.45*	Limestone	Host rock	–3.8	18.3	08-07 199.33	Dol-1	Stage 1	–0.6	18.4
08-07 17.95	Limestone	Host rock	–0.8	18.6	08-06 45.82	Dol-1	Stage 1	–5.2	19.6
10-73 275.50*	Limestone	Host rock	–2.8	19.1	09-51 74.52*	Dol-1	Stage 1	–6.7	17.5
ER-13	Limestone	Host rock	–0.6	16.2	09-67 51.30	Dol-1	Stage 1	–7.1	17.8
08-07 17.95*	Limestone	Host rock	–1.1	16.9	09-59 110.30	Dol-1	Stage 1	–6.5	17.9
08-07 41.50*	Limestone	Host rock	–3.6	17.7	10-75 176.65*	Dol-1	Stage 1	–7.8	16.3
08-07 18.73*	Limestone	Host rock	–1.4	18.3	10-73 219.50	Dol-1	Stage 1	–6.8	17.6
08-07 17.95	Limestone	Host rock	–1.2	19.1	10-75 212.35	Dol-1	Stage 1	–7.2	17.7
ER-3	Limestone	Host rock	–0.5	20.1	08-04 162.30	Dol-1	Stage 1	–7.0	17.8
ER-1	Limestone	Host rock	1.1	20.7	09-18 261.50*	Dol-1	Stage 1	–6.4	17.8
08-07 9.22	Limestone	Host rock	–0.8	20.9	10-77 121.60*	Dol-1	Stage 1	–6.8	17.8
ER-9*	Limestone	Host rock	0.7	22.1	08-07 194.93	Dol-1	Stage 1	–7.3	18.0
ER-7*	Limestone	Host rock	3.2	22.3	08-04 122.36	Dol-1	Stage 1	–7.1	18.2
Sc10-05 245.5	RP-WR	Int		11.2	09-66 67.05	Dol-1	Stage 1	–7.1	18.2
Sc10-05 221.0*	RP-WR	Int		11.6	10-89 257.00	Dol-1	Stage 1	–6.2	19.3
Sc10-05 212.00	RP-Mbl	Int	–6.5	12.9	08-07 227.64	Dol-2a	Stage 2a	–8.4	15.4
Sc10-05 216.40	RP-Mbl	Int	–1.5	18.1	08-04 122.36	Dol-2a	Stage 2a	–8.1	16.2
Sc10-05 256.30	RP-Cal	Int	–1.7	–5.2	08-04 136.45	Dol-2a	Stage 2a	–7.1	17.5
Sc10-05 260.70*	RP-Cal	Int	–4.2	17.0	10-75 212.35	Dol-2b	Stage 2b	–8.2	15.9
Sc10-05 268.70	RP-Cal	Int	–1.4	20.4	09-66 55.70	Dol-2b	Stage 2b	–6.4	17.6
10-89 103.31*	Mbl	Host rock	–3.8	13.4	10-89 104.10	Dol-2b	Stage 2b	–7.3	17.9
10-76 133.80*	Mbl	Host rock	–3.0	15.7	10-75 176.65	Dol-2b	Stage 2b	–7.0	18.0
10-77 122.15	Mbl	Host rock	–0.6	20.1	10-73 199.90*	Dol-2b	Stage 2b	–7.0	18.3
10-77 117.71	Mbl	Host rock	–1.4	20.2	08-07 212.89	Qz-3b	Stage 3b	n/a	16.9
08-05 159.35*	Mbl	Host rock	2.0	22.0	08-07 176.67	Qz-3b	Stage 3b	n/a	17
08-04 174.38	Mbl	Host rock	1.4	22.9	08-04 136.45*	Cal-4b	Stage 4b	–7.0	11.8
08-04 174-38	Mbl	Host rock	1.3	23.1	08-05 77.30	Cal-4b	Stage 4b	–7.8	14.7
08-04 174.38*	Mbl	Host rock	1.2	23.1	08-06 38.60*	Cal-4b	Stage 4b	–6.4	15.6
08-07 238.16	Lep	Host rock	–3.7	14.4	08-07 199.67	Cal-4b	Stage 4b	–6.6	15.7
10-73 408.00	Lep	Host rock	–3.9	14.6	08-04 113.96	Cal-4b	Stage 4b	5.1	16.4
08-04 181.65	Lep	Host rock	–0.6	18.9	08-07 199.33*	Cal-4b	Stage 4b	–6.6	16.4
10-87 109.60	Dol-1	Stage 1	–6.5	12.5	08-07 115.20	Cal-4b	Stage 4b	–4.4	14.8
09-66 55.70	Dol-1	Stage 1	–6.0	16.4	08-07 199.33	Cal-4b	Stage 4b	–6.7	15.5
08-07 172.74	Dol-1	Stage 1	–6.1	17.3	08-07 211.04	Cal-4b	Stage 4b	–6.9	15.8
08-04 136.45*	Dol-1	Stage 1	–7.3	17.4	08-07 119.33	Cal-4b	Stage 4b	–6.7	16
08-07 227.64	Dol-1	Stage 1	–7.3	17.6	08-07 115.20	Cal-4b	Stage 4b	–7.1	16.3
08-04 145.59	Dol-1	Stage 1	–7.5	17.7	09-18 250.25*	Cal-5	Stage 5	1.0	–1.3
08-07 199.67	Dol-1	Stage 1	–7.4	17.7	10-89 123.30	Cal-5	Stage 5	–4.4	2.7
08-04 136.45	Dol-1	Stage 1	–7.1	17.8	10-89 123.30	Cal-5	Stage 5	–2.8	3.4
08-07 199.33*	Dol-1	Stage 1	–3.3	17.8	10-99 475.00*	Cal-5	Stage 5	–2.7	4.0
08-07 175.46	Dol-1	Stage 1	–7.4	18.1	09-18 256.74*	Cal-5	Stage 5	–2.9	16.0
08-07 217.77	Dol-1	Stage 1	–7.2	18.3					

Sample IDs with asterisks (*) correspond to samples that have also been analyzed for ^{87}Sr/^{86}Sr
Abbreviations: Cal = calcite, Dol = dolomite, Int = intrusion, Lep = leopard marble, Lst = limestone, Mbl = marble, Qz = quartz, RP = Rackla pluton, RP-cal = Rackla pluton-hosted calcite vein, WR = whole rock

units), and low ferric/ferrous iron ratios (~0.2–0.3). However, they also have a general northwest to southeast trend of relatively oxidized to reduced, metaluminous to peraluminous, younger to older, and gold-rich to more tungsten rich systems (Hart et al., 2004). The Rackla pluton has high δ^{18}O values (~+11), low magnetic responses (Dumala, 2010, 2011), ferric/ferrous ratios below 0.5 (Fig. 9), is highly peraluminous, and has associated tungsten mineralization (Kingston et al., 2010); thus, it closely resembles magma compositions of the southeastern tungsten-rich/gold-poor Tungsten plutonic suite (Hart et al., 2004). The very reduced nature of the Rackla pluton is unusual when compared to other Tombstone-Tungsten magmatic belt intrusions to the southwest. However, the platformal rocks north of the Dawson thrust vary considerably from Selwyn Basin rocks to the south; thus, the nature of the host rocks may have had a role in determining the reduced nature of the Rackla pluton.

Three types of marble occur in the study area: one in the Rackla pluton thermal aureole, one in the sheared Tiger fault, and the third within the Tiger deposit. The Tiger deposit marble is localized along rheologic boundaries above and below volcanic horizons and is rarely more than 4 m thick; therefore, it is suggested to be a product of fracture-controlled, local fluid-mediated metasomatism. Collectively, the marbles show a broad positive correlation in δ^{13}C and δ^{18}O values (Fig. 12); one end-member has isotopic compositions similar to some of the least altered host limestones, while the other end-member is closer to the most altered host limestone values. The Rackla pluton aureole marble and leopard unit calcite have the lowest δ^{13}C and δ^{18}O values, with the former having values of –6.5 and 12.9‰, respectively. The ^{87}Sr/^{86}Sr values for the Tiger deposit marble range from 0.70933 to 0.71626 and, like in the limestones, the ^{87}Sr/^{86}Sr values deviate from Ordovician to Silurian normal marine values and are correlated with more

Table 4. All δ^{34}S Values for Tiger Deposit and Rackla Pluton Samples

Sample ID	Phase	Stage	δ^{34}S (‰)	Sample ID	Phase	Stage	δ^{34}S (‰)
09-66 67.40	Apy-1	Stage 1	7.3	10-89 268.45	Py-2b	Stage 2b	1.7
08-04 162.30	Apy-1	Stage 1	7.4	10-89 251.88	Py-2b	Stage 2b	7.2
09-66 67.05	Apy-1	Stage 1	7.6	08-09 156.24	Py-2b	Stage 2b	7.4
09-66 69.90	Apy-1	Stage 1	7.7	08-04 162.30	Py-2b	Stage 2b	7.5
08-04 168.26 b	Apy-1	Stage 1	7.8	08-04 156.24	Py-2b	Stage 2b	7.7
08-07 227.64	Apy-1	Stage 1	7.9	08-07 227.47	Py-2b	Stage 2b	7.8
08-04 163.64 a	Apy-1	Stage 1	7.9	08-04 166.16	Py-2b	Stage 2b	8.4
10-77 121.60 a	Apy-1	Stage 1	7.9	08-07 216.74	Py-3a	Stage 3a	3.4
09-67 51.30	Apy-1	Stage 1	8.0	09-18 238.10 a	Py-3a	Stage 3a	3.5
10-75 132.90	Apy-1	Stage 1	8.0	10-75 201.0	Py-3a	Stage 3a	3.5
08-05 102.80	Apy-1	Stage 1	8.0	10-87 266.90	Py-3a	Stage 3a	3.6
08-04 168.26 a	Apy-1	Stage 1	8.2	08-18 238.10 c	Py-3a	Stage 3a	4.0
08-05 77.30 b	Apy-1	Stage 1	8.3	09-18 238.10 b	Py-3a	Stage 3a	4.3
10-77 121.60 b	Apy-1	Stage 1	8.3	09-18 232.00	Py-3a	Stage 3a	4.3
10-77 121.0	Apy-1	Stage 1	8.4	08-06 75.68	Py-3a	Stage 3a	4.9
08-04 122.36	Apy-1	Stage 1	8.4	08-07 209.05 a	Py-3a	Stage 3a	5.1
08-04 163.64 b	Apy-1	Stage 1	8.5	08-07 216.74	Py-3a	Stage 3a	5.4
08-06 24.95	Apy-1	Stage 1	8.6	09-59 30.05	Py-3a	Stage 3a	6.1
08-05 77.30 a	Apy-1	Stage 1	8.6	08-07 209.05 b	Py-3a	Stage 3a	6.6
08-09 116.74	Apy-1	Stage 1	8.7	08-07 209.30	Py-3a	Stage 3a	7.0
09-59 37.90	Apy-1	Stage 1	8.7	09-59 110.30	Py-3a	Stage 3a	7.4
08-07 174.13	Apy-1	Stage 1	8.7	09-18 257.70	Py-3a	Stage 3a	7.5
08-04 111.66	Apy-1	Stage 1	8.8	09-18 256.24	Py-3a	Stage 3a	7.6
08-07 174.55	Apy-1	Stage 1	8.9	10-75 132.90	Py-3a	Stage 3a	7.9
08-07 174.13	Apy-1	Stage 1	8.9	10-89 112.85	Py-3a	Stage 3a	8.3
08-07 175.80	Apy-1	Stage 1	8.9	08-05 71.55	Py-3a	Stage 3a	8.4
08-07 176.67	Apy-1	Stage 1	8.9	09-18 250.00	Py-3a	Stage 3a	8.4
10-87 113.40 a	Apy-1	Stage 1	8.9	09-51 74.52	Py-3a	Stage 3a	8.5
10-87 113.40 b	Apy-1	Stage 1	8.9	09-18 269.55	Py-3a	Stage 3a	8.6
08-04 116.74	Apy-1	Stage 1	9.0	08-04 111.66	Py-3a	Stage 3a	8.8
08-07 174.62	Apy-1	Stage 1	9.0	10-73 177.40	Py-3a	Stage 3a	8.9
08-04 113.24	Apy-1	Stage 1	9.2	09-18 250.25	Py-3a	Stage 3a	9.0
10-75 176.65	Py-2a	Stage 2a	5.0	09-18 263.70	Py-3a	Stage 3a	9.6
08-05 102.80	Py-2a	Stage 2a	6.5	09-18 232.00	Bs-3c	Stage 3c	3.4
08-07 199.67	Py-2a	Stage 2a	6.6	10-89 247.20	Po-3c	Stage 3c	3.5
09-66 5570	Py-2a	Stage 2a	7.0	08-04 111.66	Bs-3c	Stage 3c	4.5
09-67 12.40	Py-2a	Stage 2a	7.2	10-87 268.10 a	Po-3c	Stage 3c	4.9
08-04 160.51	Py-2a	Stage 2a	7.2	10-73 177.40	Po-3c	Stage 3c	4.9
09-67 51.30	Py-2a	Stage 2a	7.4	09-59 30.05	Po-3c	Stage 3c	5.1
09-66 67.40	Py-2a	Stage 2a	7.5	10-87 268.10 b	Po-3c	Stage 3c	5.9
09-66 69.90	Py-2a	Stage 2a	7.6	08-06 38.60	Po-3c	Stage 3c	6.2
08-07 199.33	Py-2a	Stage 2a	7.8	08-05 71.55	Po-3c	Stage 3c	8.6
08-07 214.30	Py-2a	Stage 2a	7.8	09-18 256.24	Sp-4a	Stage 4a	−1.2
10-77 121.60	Py-2a	Stage 2a	8.0	09-18 257.70	Sp-4a	Stage 4a	4.1
10-87 109.60	Py-2a	Stage 2a	8.0	09-18 250.0	Sp-4a	Stage 4a	4.6
08-09 116.76	Py-2a	Stage 2a	8.0	Sc10-05 268.70 a	Sp-4a	Stage 4a	5.1
09-66 67.05	Py-2a	Stage 2a	8.1	Sc10-05 268.70 b	Sp-4a	Stage 4a	5.2
08-06 45.82	Py-2a	Stage 2a	8.5	Sc10-05 268.70 a	Apy	Int	6.0
08-05 77.30	Py-2a	Stage 2a	8.5	Sc10-05 268.70 b	Apy	Int	6.3
10-77 121.0	Py-2a	Stage 2a	8.6	Sc10-05 268.70 a	Py	Int	6.4
10-87 113.40	Py-2a	Stage 2a	8.8	Sc10-05 268.70 b	Py	Int	6.6

Abbreviations: Apy = arsenopyrite, Bs = bismuthinite, Po = pyrrhotite, Py = pyrite, Sp = sphalerite

negative δ^{13}C and δ^{18}O values (Fig. 14). Because the trend of the isotopic composition of the aureole marble is almost certainly a product of intrusion-related metasomatism, it is likely that the mimicking of isotopic trends present in the host limestones and Tiger deposit marble is also a product of Rackla pluton-related fluid interaction with the host rock.

Evolution of the magmatic hydrothermal system in the Rackla pluton

The FIAs hosted in magmatic quartz appear to be primary, but CL was not performed on this sample and, therefore, this cannot be definitely confirmed. Microthermometric data are limited for the Rackla pluton and, thus, only general comments will made here. Inclusion types hosted in magmatic quartz in the Rackla pluton include liquid water + carbonic liquid, liquid water + carbonic liquid + solid halite, liquid water + water vapor, liquid water + water vapor + solid halite, and secondary liquid water + water vapor whereas primary inclusions in crosscutting calcite veins only contain liquid water + water vapor compositions. Although the absolute timing of these inclusions remains unclear, the secondary trails in the quartz and primary inclusions in the crosscutting
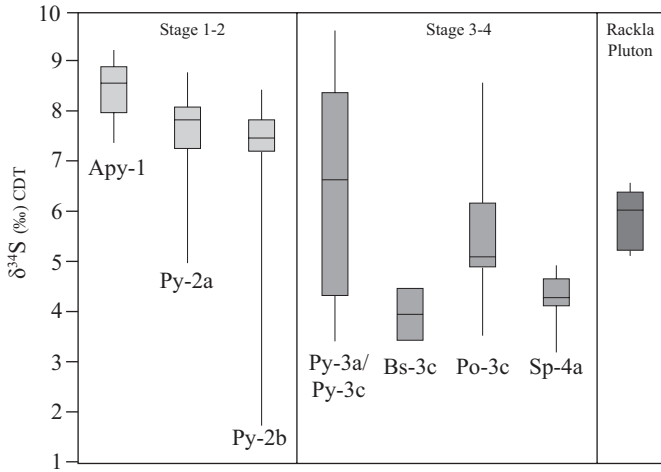
Fig. 13. $\delta^{34}S$ values for Tiger deposit and Rackla pluton sulfides with respect to paragenesis.

calcite veins have similar aqueous compositions, suggesting there was an earlier phase of saline aqueous-carbonic fluid (a higher-temperature event), followed by a later aqueous (lower-temperature) event. No unequivocal unmixing assemblages were observed, although the earlier fluid event has FIA compositional similarities to Tiger deposit dolomite 1, dolomite 2a, and quartz 3b. The temperature of first ice melting (T_{FM}) for the aqueous phase in all the inclusions ranges between –33° and –22°C and may indicate the presence of some divalent ions in addition to NaCl in the fluids (Crawford, 1981), which is also a characteristic of Tiger deposit fluids (see

below). Salinity data from FIAs have a broadly bimodal distribution with halite-bearing inclusions ranging from 27 to 40 wt % NaCl equiv with a mode at 30 wt % NaCl equiv. No clathrate was observed in the nonhalite-bearing aqueous-carbonic inclusions, so the calculated salinity values are overestimated (e.g., Diamond, 1994) but have salinities that are less than 17 wt % NaCl equiv. Total T_H range from 200° to 300°C for the noncarbonic inclusions, including the trail-hosted liquid water + water vapor inclusions, while the carbonic inclusions have higher T_H, from 300° to 420°C. Overall, the higher-temperature, CO_2-bearing inclusions predate the cooler, trail-hosted, aqueous inclusions; thus, the cooler aqueous inclusions may represent the ingress of meteoric fluids into the pluton during the waning of the magmatic-hydrothermal system.

Meteoric fluid ingress is supported by isotopic and

Table 5. Strontium Isotope Data for Tiger Deposit and Rackla Pluton Samples

Sample ID	Type	Stage	Sr (ppm)	$^{87}Sr/^{86}Sr$	±2 SE
ER-7	Lst	Host rock	271.4	0.70858	0.00003
ER-9	Lst	Host rock	295.4	0.70924	0.00002
08-07 18.73	Lst	Host rock	51.28	0.71318	0.00004
08-07 17.95	Lst	Host rock	53.14	0.71347	0.00002
08-07 61.45	Lst	Host rock	49.11	0.71694	0.00002
10-73 275.50	Lst	Host rock	69.68	0.72050	0.00002
08-07 41.50	Lst	Host rock	23.86	0.72642	0.00004
Sc10-05 260.70	RP-Cal	Int	3.343	0.72926	0.00014
08-04 174.38	Mbl	Host rock	110.3	0.70933	0.00002
10-76 133.80	Mbl	Host rock	408.9	0.71205	0.00004
10-89 103.31	Mbl	Host rock	138.4	0.71626	0.00002
08-05 159.35	Mbl-Cal	Host rock	151.5	0.71104	0.00002
08-07 199.33	Dol-1	Stage 1	61.90	0.71834	0.00002
09-51 74.52	Dol-1	Stage 1	87.29	0.72039	0.00002
10-75 176.65	Dol-1	Stage 1	123.5	0.72182	0.00002
09-18 261.50	Dol-1	Stage 1	104.0	0.72185	0.00005
08-04 136.45	Dol-1	Stage 1	113.0	0.72349	0.00003
10-77 121.60	Dol-1	Stage 1	105.3	0.72439	0.00004
10-73 199.90	Dol-2a	Stage 2a	133.9	0.72520	0.00002
08-06 38.60	Cal-4b	Stage 4b	73.50	0.71894	0.00002
08-04 136.45	Cal-4b	Stage 4b	75.69	0.71954	0.00003
08-07 199.33	Cal-4b	Stage 4b	36.65	0.72821	0.00003
09-18 256.24	Cal-5	Stage 5	326.7	0.71701	0.00002
09-18 250.25	Cal-5	Stage 5	42.93	0.71837	0.00004
10-99 475.00	Cal-5	Stage 5	36.17	0.71889	0.00002

Abbreviations: Cal = calcite, Dol = dolomite, Int = intrusion, Lst = limestone, Mbl = marble, RP-Cal = Rackla pluton-hosted calcite vein
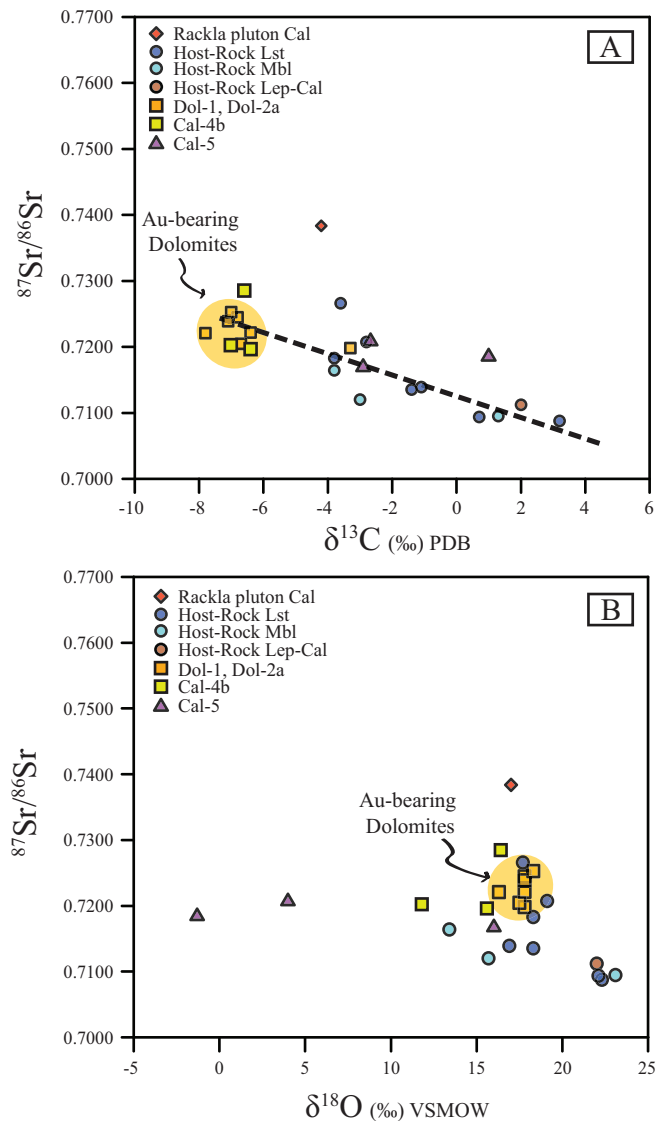

Fig. 14. A) $^{87}Sr/^{86}Sr$ vs. $\delta^{13}C$ values of Tiger deposit host rocks, hydrothermal mineralization, and Rackla pluton vein calcite showing a general increase in $^{87}Sr/^{86}Sr$ and a decrease in $\delta^{13}C$ values relative to unaltered host rocks. B) $^{87}Sr/^{86}Sr$ data vs. $\delta^{18}O$ values showing a slight increase in $^{87}Sr/^{86}Sr$ with a decrease in $\delta^{18}O$ values from unaltered host rocks.

microthermometric data from the late calcite veins that cross-cut the pluton. These veins contain primary aqueous fluid inclusions with salinities of 16 wt % NaCl equiv and homogenization temperatures of 280°C and are comparable to the trail-hosted secondary inclusions hosted in the Rackla pluton quartz. Furthermore, one of the calcite vein samples has a negative $\delta^{18}O$ value (Fig. 12, Table 3), which requires a component of meteoric water. Two other vein calcites have $\delta^{13}C$ and $\delta^{18}O$ values similar to those of the limestone host rocks. A $^{87}Sr/^{86}Sr$ value of 0.72926, for the calcite vein with a negative $\delta^{18}O$ value, is much higher than other limestone host rocks and marbles. The elevated $^{87}Sr/^{86}Sr$ values, variable $\delta^{13}C$ and $\delta^{18}O$ values, and fluid inclusion homogenization temperatures, therefore, suggest that these veins (and the secondary inclusions in the magmatic quartz) are derived from mixed magmatic-meteoric hydrothermal circulation or from meteoric water that variably equilibrated with an elevated $^{87}Sr/^{86}Sr$ reservoir.

Evolution of the Tiger deposit mineralization

Early gold-bearing mineralization within the Tiger deposit occurs as lattice-bound, arsenopyrite-hosted gold, associated with abundant replacive dolomite and lesser pyrite. The foliation-parallel growth of pyrite 2a, dolomite 2a, and arsenopyrite 2a postdates the first gold-bearing event, suggesting that, at the property scale, the rocks have been deformed in a ductile manner. Some samples of dolomite 1, 2a, and 2b are twinned and may have undergone a minor amount of plastic deformation. The mechanisms and degree of deformation in these dolomites are beyond the scope of this study; however, dolomite deformation can occur in a ductile manner at low temperatures (~380°C) by accommodation through dislocation glide and mechanical twinning (Turner et al., 1954; Davis et al., 2008). Foliated mineral growth postdates dolomite 1 and arsenopyrite 1 mineralization and is not associated with significant gold precipitation. The prestrain fluids pervasively replaced the carbonate host rocks, with the highest gold grades occurring along the rheologic boundaries on the margins of the volcanic packages and the host carbonates, possibly due to higher fluid flow rates or more reactive rocks in these locations.

The minerals associated with the first gold mineralizing event, specifically dolomite 1, 2a, and 2b, have low $\delta^{13}C$ and low $\delta^{18}O$ values compared to the host limestones and marbles and occur as a tight cluster with a weak trend (Fig. 12). Importantly, the gold-hosting dolomites do not occur directly on the linear trend formed by altered host-rock values. Additionally, the $^{87}Sr/^{86}Sr$ values for dolomite 1, dolomite 2a, and calcite 4b have a narrow range (0.71701–0.72520) and show generally higher $^{87}Sr/^{86}Sr$ than the host limestones and marbles. The data suggest that potentially two distinct fluid compositions contributed to the trends defined by the host rocks and the dolomites. To test whether the isotopic trends present in the limestones and hydrothermal minerals were formed by the same fluid, a theoretical two-component $^{87}Sr/^{86}Sr$ mixing line (Faure and Mensing, 2005; Fig. 15) between an unaltered limestone end-member and an end-member with high $^{87}Sr/^{86}Sr$ is modeled. To obtain this isotopic trend, a high $^{87}Sr/^{86}Sr$ isotopic end-member would be required to mix with unaltered limestone $^{87}Sr/^{86}Sr$ isotopic compositions. Such high $^{87}Sr/^{86}Sr$ values exist in Precambrian sedimentary rocks
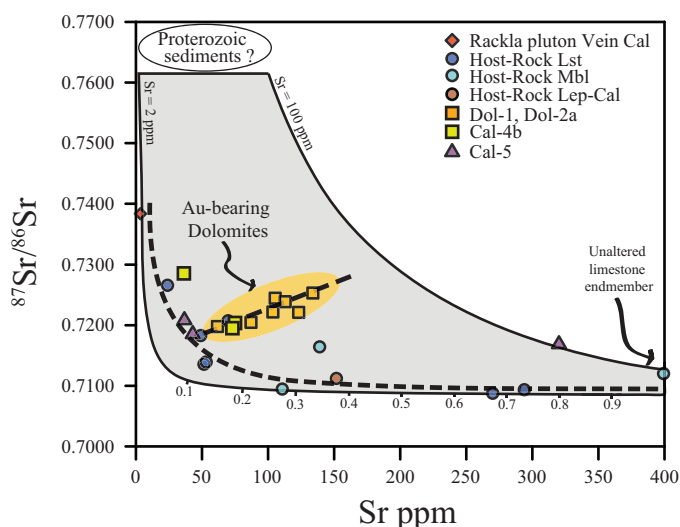

Fig. 15. Modeled mixing of a two-component system with end-members represented by unaltered limestone ($^{87}Sr/^{86}Sr$ = 0.7086–0.7120, Sr = 400 ppm) and a hypothetical Proterozoic sedimentary source ($^{87}Sr/^{86}Sr$ > 0.7600, Sr = 2–100 ppm). Annotated numbering denotes the weight ratio degree of mixing between the two end-members; for 0.9, 10% of the high ^{87}Sr source has mixed with 90% of the unaltered limestone source. The host rocks display an isotopic trend different from that of the gold-hosting dolomites.

of southern Yukon and northern British Columbia (Driver et al., 2000) and, although untested, Proterozoic sedimentary rocks also occur adjacent to the Tiger deposit study area (Fig. 2) and therefore may contain high $^{87}Sr/^{86}Sr$ values. The majority of marbles and Tiger deposit carbonates fall within the modeled mixing zone, and only 10 to 30% mixing of the high $^{87}Sr/^{86}Sr$ isotopic signature is needed to produce the values within the Tiger deposit carbonates and the altered host-rock limestones and marbles (Fig. 15). However, two clear trends occur within this modeled mixing zone as well. One is the negative hyperbolic slope defining the host rocks, and the second is the positive linear slope defining the gold-hosting dolomites and calcite 4b. Therefore, the isotopic signatures in the host rock likely formed from a fluid distinct from the later gold-bearing mineralizing phases. Coupled $\delta^{18}O$ and $\delta^{13}C$ isotopic depletions as presented in Figure 12 are well documented within contact metamorphic carbonate aureoles and are attributed to metasomatic fluid-rock isotopic exchange (Valley, 1986; Baumgartner and Valley, 2001). Baumgartner and Valley (2001) suggest that shifts from normal marine values to igneous values with $\delta^{13}C$ and $\delta^{18}O$ values of ~–7 and +7, respectively, indicate large volumes of magmatic water fluid flow, whereas $\delta^{18}O$ shifts approaching 0‰ indicate interaction with meteoric waters. Because the two isotopic trends in the Tiger data have minimum $\delta^{18}O$ values of ~13‰ and are no lower than Rackla pluton whole-rock values of ~11‰, they are likely a product of magmatic water interaction and not meteoric water. Thus, an early, possibly lower temperature, nonmineralizing fluid may have altered the host limestones/dolostones and formed Tiger marble and Rackla pluton aureole marble locally. A second distinct, higher-temperature, gold-mineralizing fluid that formed the replacement dolomite 1, 2a, 2b, arsenopyrite 1, and calcite 4b spatially and isotopically overprinted the early paragenetic stage limestones and

marbles. Both of these fluids are likely related to the Rackla pluton or a related source at depth.

The stage 1 sulfide assemblage of arsenopyrite 1, pyrite 2a, and pyrite 2b has a narrow range of $\delta^{34}S$ values centered around 8‰. Only pyrite 3a/pyrite 3c has a bimodal sulfur isotope distribution reflecting two stages of pyrite growth, which were not resolved at the scale of the sampling. Pyrrhotite 3c, bismuthinite 3c, and sphalerite 4a have $\delta^{34}S$ values of 3.4 to 6.2‰, with one value of 8.6‰. These values later in the paragenesis are lower than the earlier sulfides. A decrease in $\delta^{34}S$ values later in the paragenesis cannot be due to cooling of a single hydrothermal fluid because the $\delta^{34}S$ values should increase with cooling (Rye and Ohmoto, 1974). More likely, mixing of Rackla pluton primary $\delta^{34}S$ values (~6‰) with sedimentary sulfates (>10‰, Claypool et al., 1980; Cecile et al., 1983) would produce $\delta^{34}S$ values of ~8‰ as in the early sulfides. Conversely, mixing with biogenic sediments (<0‰) could produce the values of <6‰ seen in the later sulfide phases. Furthermore, the proximity of Selwyn Basin metasediments and local barite occurrences suggests that the local country rocks contain variable sulfur isotope source compositions, which may be reflected in the range of $\delta^{34}S$ values in the Tiger deposit sulfides. These variable sulfur isotope compositions may be due to complex fluid migration pathways and/or more complex subsurface geology than presently known.

Lead isotopes in undifferentiated pyrite and pyrrhotite within Tiger deposit mineralization were analyzed by Kingston et al. (2010). The $^{207}Pb/^{204}Pb$ values range from 15.596 to 15.940 and the $^{206}Pb/^{204}Pb$ ratios from 19.105 to 21.046. Although there is considerable scatter in their dataset, the results indicate that the Pb isotope compositions of Tiger deposit sulfides more closely resemble those of the Rackla pluton than the Tombstone intrusions.

Detailed modeling of the fluid inclusion data could not be carried out because of decrepitation during heating runs and the lack of clathrate data from CO_2-bearing inclusions (Diamond, 1994). Furthermore, there are presently no equations of state that adequately describe CO_2-bearing halite-saturated brines. Primary FIAs of carbonic liquid + liquid water and liquid water + carbonic liquid + solid halite + solid opaque in dolomite 1, dolomite 2b, and quartz 3b have bimodal salinities of less than 16 wt % NaCl equiv and between 30 and 35 wt % NaCl equiv, respectively. Decrepitation temperatures in dolomite 1 and quartz 3b for these FIAs range between 230° and 440°C, and a small number of T_H for liquid water + carbonic liquid + solid halite + solid opaque inclusions are recorded at 350° to 411°C. The vast majority of fluid inclusions in dolomite 1, dolomite 2b, and quartz 3b are aqueous-carbonic (carbonic liquid + liquid water) and are associated with gold-bearing mineralization. However, the FIAs containing carbonic liquid + liquid water and liquid water + carbonic liquid + solid halite + solid opaque are coeval and represent varying degrees of fluid immiscibility. Rare liquid water + carbonic liquid fluid inclusions occur coevally within immiscible FIAs of carbonic liquid + liquid water and liquid water + carbonic liquid + solid halite + solid opaque and resemble a fluid of intermediate composition, which is possibly a mixed fluid of the immiscible assemblage. Carbon dioxide is the most common magmatic volatile after H_2O and, due to its low solubility in magmas, it will exsolve at deeper levels than H_2O

(Baker, 2002). Carbon dioxide readily enters the vapor phase of immiscible aqueous fluids and its molar proportions can be used as a rough proxy for depth of exsolution with the magma; higher proportions of CO_2 (50% or more) in the vapor phase may correspond with pressures of ~3 kbar or depths of ~9 km at 750°C, and minor CO_2 in the vapor phase may correspond with <1-kbar pressure or ~3-km depth (Lowenstern, 2001). Carbon dioxide inclusions in dolomite 1, dolomite 2a, dolomite 2b, and quartz 3b have high degrees of fill (~0.95) and occur in the liquid state at ambient temperatures, indicating a relatively deep level of exsolution and trapping of approximately 3- to 9-km depth. The fluid inclusion characteristics and interpreted depths and temperatures of mineralization are similar to mid- to deep-level IRGDs such as Fort Knox or the Eagle gold deposit, yet they do not occur in the sheeted veins (Baker, 2002).

Benning and Seward (1996) have shown gold can be transported in near-neutral pH, H_2S-bearing fluids by bisulfide complexing. Additionally, it has been suggested that gold, arsenic, and sulfur partition into the vapor phase during fluid immiscibility (Heinrich et al., 1999). It is possible, therefore, that CO_2 exsolution promoted metal (Au, As, S) partitioning into the vapor phase as bisulfide compounds, which subsequently interacted with iron in the host volcanic rocks and precipitated gold and arsenic within arsenopyrite 1. The invisible nature of this gold implies the mineralizing fluid did not reach gold saturation.

The second gold-bearing event (gold 3c) is distinct, as there is no arsenopyrite or significant dolomite formed. Rather, gold 3c, bismuthinite 3c, and pyrrhotite 3c occur in brittle fractures of earlier sulfides and are associated with stage 4 base metal mineralization. Since these mineral assemblages postdate quartz 3b, there are no fluid inclusion data that directly relate to them; however, it is clear that, from quartz 3b to calcite 5, the temperature decreased from approximately 400° to 150°C. The temperature decrease at the end of the paragenesis suggests that possible dilution and cooling of the magmatic fluids by meteoric fluids may have resulted in the base metals precipitating from solution. Because the second gold-bearing event contains a distinct mineral assemblage (gold 3c, bismuthinite 3c, and pyrrhotite 3c) in brittle fractures within sulfide grains, it likely precipitated by a different mechanism than the first gold-bearing event. Also, the nature of the fracture-hosted gold indicates brittle deformation was more pervasive in the second gold-bearing event, suggesting a lower-pressure or -temperature environment. Therefore, this second gold-bearing event may have resulted from destabilization of bisulfide complexes in the CO_2-rich carbonic liquid + liquid water fluids through depressurizing, cooling, and/or mixing with meteoric water. Depressurization could have occurred through transient zones of dilatancy through episodic movement of the property-scale shear zone.

Meteoric input and collapse of the hydrothermal system

The $\delta^{13}C$ and $\delta^{18}O$ values for calcite 5 are similar to the isotopic values of the late calcite veins cutting the Rackla pluton (Fig. 12); however, the $^{87}Sr/^{86}Sr$ values for this calcite are lower than those of the Rackla pluton calcite veins. The low $\delta^{18}O$ values in calcite 5 are diagnostic of a meteoric water component, which overprints the mineralization and likely
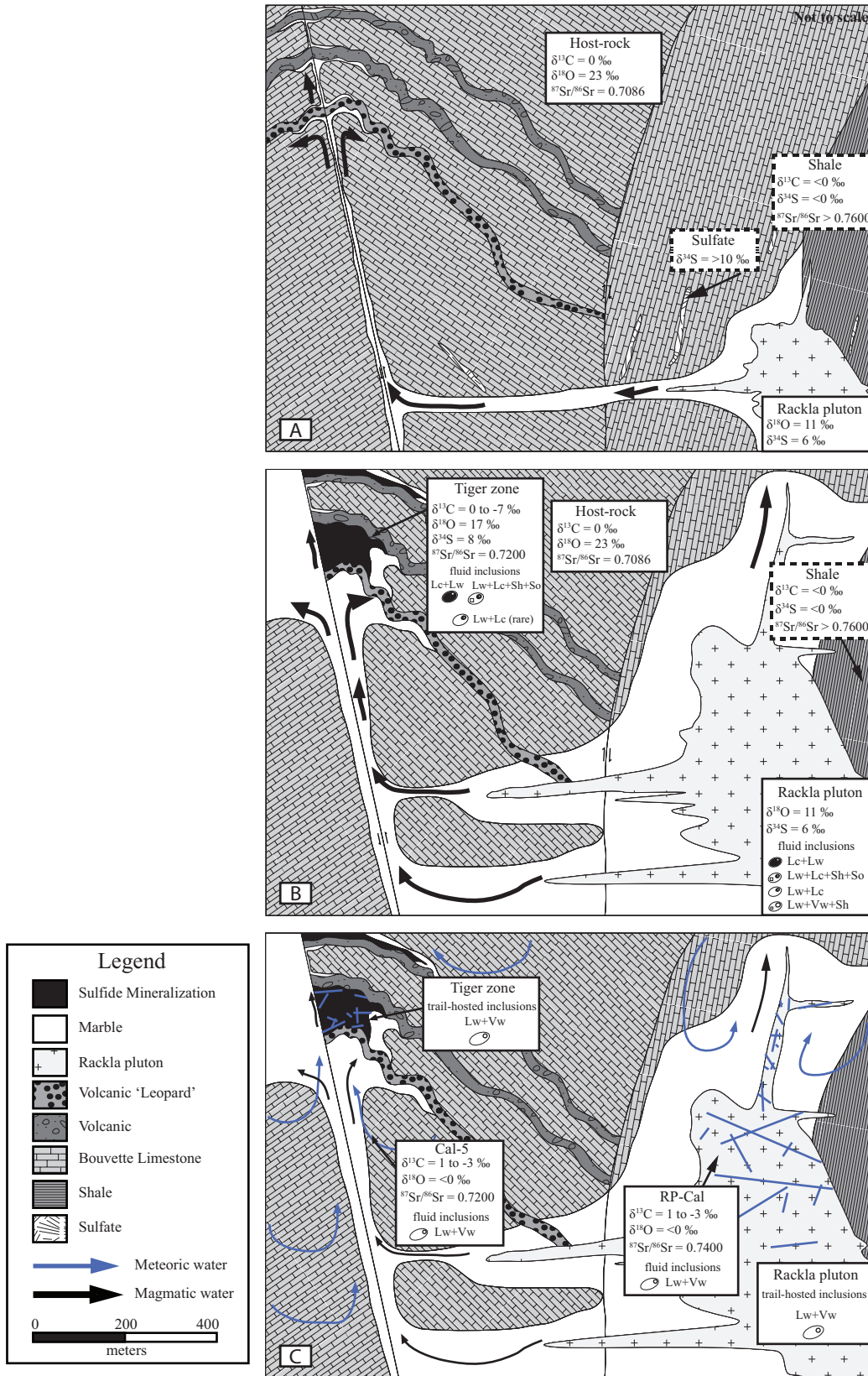
Fig. 16. Genetic diagram for Tiger deposit mineralization. Figure is not to scale. A) Rackla pluton emplacement and formation of aureole and Tiger deposit marble via a distinct magmatic hydrothermal fluid. Fluids follow structural and rheologic boundaries. B) Significant fluid flow occurs as the magmatic-hydrothermal system develops, forming Tiger deposit mineralization from ~400°C fluids. C) Ingress of meteoric waters occurs as magmatic-hydrothermal activity wanes.

forms the late calcite veins in the Rackla pluton; however, the lower $^{87}Sr/^{86}Sr$ values in the calcite 5 veins may be due to less water-rock interaction with the high $^{87}Sr/^{86}Sr$ reservoir due to distance from the heat source.

Secondary fluid inclusion trails in sphalerite 4a associated with calcite 5 may represent the calcite 5-forming fluid. These fluids have salinities ranging from 3 to 8 wt % NaCl equiv, are not CO_2 bearing, and have lower homogenization temperatures of 150° to 153°C and, thus, they are distinct from the primary FIAs in the Tiger deposit. The lack of CO_2, low salinity, relatively low homogenization temperatures, and low $\delta^{18}O$ values suggest this fluid has a distinct meteoric component that overprints Tiger deposit mineralization and may represent the collapse of the magmatic-hydrothermal system.

Genetic Model and Conclusions

The Tiger gold deposit occurs 7 km northeast of the Dawson thrust as strata-bound carbonate-replacement gold mineralization within the unmetamorphosed Mackenzie Platform. The nature and style of mineralization, as well as geochemical and age relationships, suggest that the Tiger gold deposit is distally (3 km) related to the Rackla pluton. Early magmatic fluids from the Rackla pluton or a related source at depth were focused by local faults and circulated through the host sedimentary rocks (Fig. 16a), resulting in the subsequent deposition of isotopically altered limestone/dolostones and marble. Hotter and chemically distinct magmatic fluids later formed dolomite, gold-bearing arsenopyrite, and pyrite (Fig. 16b) at depths of ~3 to 9 km. These fluids were largely focused along local rheologic boundaries and faults and caused increased gold grades at lithological contacts. The early arsenopyrite-hosted, gold-bearing event formed from a high-temperature (~350°C), immiscible, CO_2-bearing fluid sourced from the Rackla pluton, and precipitated due to possible reactions with iron in the host rocks or during fluid unmixing. The second gold-bearing event contains fracture-hosted free gold, bismuthinite, and pyrrhotite and may have formed from cooling and mixing with a meteoric fluid, prompting mineralization. A small amount of base metals and low-temperature calcite veining occurs late in the paragenesis and documents the influx of meteoric water and the collapse of the magmatic-hydrothermal system (Fig. 16c).

Strata-bound, fault-controlled hydrothermal mineralization of the Tiger deposit represents a distal expression of Paleocene magmatic activity in central Yukon not commonly observed in IRGDs. The occurrence of the Tiger deposit, in addition to the recently discovered Carlin-style Yukon gold (~74–43 Ma; Tucker, 2015), indicates that other significant Paleocene-aged gold resources may occur regionally adjacent to the Dawson thrust. Exploration, therefore, should not be restricted to the well-known 90 to 100 Ma Tombstone-Tungsten magmatic belt or spatially to the Selwyn Basin. Additionally, the Rackla pluton has ages, composition, and spatial proximity similar to the poorly studied McQuesten suite intrusions, indicating a potential genetic link and a neglected prospective target for gold mineralization.

Acknowledgments

REFERENCES

Abbott, G., 1990, Preliminary results of the stratigraphy and structure of the Mt. Westman map area, central Yukon: Geological Survey of Canada, Paper 90-1E, p. 15–22.

Abbott, J.G., Gordey, S.P., and Tempelman-Kluit, D.J., 1986, Setting of stratiform, sediment-hosted lead-zinc deposits in Yukon and northeastern British Columbia: Geological Survey of Canada Open File 2169, p. 69–98.

Aitken, J.D., and McMechan, M.E., 1992, Middle Proterozoic assemblages, chapter 5, in Gabrielse, H., and Yourath, C.J., eds., Geology of the Cordilleran orogen in Canada: Ottawa, Ontario, Geological Survey of Canada, p. 97–124.

Baker, T., 2002, Emplacement depth and carbon dioxide-rich fluid inclusions in intrusion-related gold deposits: Economic Geology, v. 97, p. 1111–1117.

Baker, T., and Lang, J., 2001, Fluid inclusion characteristics of intrusion-related gold mineralization, Tombstone-Tungsten magmatic belt, Yukon Territory, Canada: Mineralium Deposita, v. 36, p. 563–582.

Baumgartner, L.P., and Valley, J.W., 2001, Stable isotope transport and contact metamorphic fluid flow: Reviews in Mineralogy and Geochemistry, v. 43, p. 415–467.

Benning, L.G., and Seward, T.M., 1996, Hydrosulfide complexing of Au(I) in hydrothermal solutions from 150–400°C and 500–1500 bar: Geochimica et Cosmochimica Acta, v. 60, p. 1849–1871.

Bodnar, R.J., 1993, Revised equation and table for determining the freezing point depression of H_2O-NaCl solutions: Geochimica et Cosmochimica Acta, v. 57, p. 683–684.

Boyle, R.W., Wanless, R.K., and Stevens, R.D., 1970, Sulfur isotope investigation of the lead-zinc-silver-cadmium deposits of the Keno Hill-Galena Hill area, Yukon, Canada: Economic Geology, v. 65, p. 1–10.

Brown, I.J., and Nesbitt, B.E., 1987, Gold-copper-bismuth mineralization in hedenbergitic skarn, Tombstone Mountains, Yukon: Canadian Journal of Earth Sciences, v. 24, p. 2362–2372.

Buzon, M.R., Simonetti, A., and Creaser, R.A., 2007, Migration in the Nile Valley during the New Kingdom period: A preliminary strontium isotope study: Journal of Archaeological Science, v. 34, p. 1391–1401.

Cecile, M.P., Shakur, M.A., and Krouse, H.R., 1983, The isotopic composition of western Canadian barites and the possible derivation of oceanic sulfate $\delta^{34}S$ and $\delta^{18}O$ age curves: Canadian Journal of Earth Sciences, v. 20, p. 1528–1535.

Claypool, G.E., Holser, W.T., Kaplan, I.R., Sakai, H., and Zak, I., 1980, The age curves of sulfur and oxygen isotopes in marine sulfate and their mutual interpretation: Chemical Geology, v. 28, p. 199–260.

Clayton, R.N., and Mayeda, T.K., 1963, The use of bromine pentafluoride in the extraction of oxygen from oxides and silicates for isotopic analysis: Geochimica et Cosmochimica Acta, v. 27, p. 43–52.

Colpron, M., Moynihan, D., Israel, S., and Abbott, G., 2013, Geological map of the Rackla belt, east-central Yukon (NTS 106C/1-4, 106D/1): Yukon Geological Survey, Open File 2013-13, scale 1:50,000, 5 maps and legend.

Crawford, M.L., 1981, Phase equilibria in aqueous fluid inclusions: Mineralogical Association of Canada Short Course Handbook 6, p. 75–100.

Davis, N.E., Kronenberg, A.K., and Newman, J., 2008, Plasticity and diffusion creep of dolomite: Tectonophysics, v. 456, p. 127–146.

Diamond, L.W., 1994, Introduction to phase relations of CO_2-H_2O fluid inclusions, in De Vito, B., and Frezzotti, M.L., Fluid inclusions in minerals: Methods and applications, IMA '94, Short Course: Blacksburg, VA, Virginia Tech, Fluids Research Laboratory, p. 376.

Driver, L.A., Creaser, R.A., Chacko, T., and Erdmer, P, 2000, Petrogenesis of the Cretaceous Cassiar batholith, Yukon-British Columbia, Canada: Implications for magmatism in the North American Cordilleran Interior: GSA Bulletin, v. 112, p. 1119–1133.

Dumala, M., 2010, Assessment report describing geophysics, soil geochemistry and diamond drilling at the Rau property: Prepared for ATAC Resources, ltd.http://virtua.gov.yk.ca:8080/lib/item?id=chamo:166448&theme=emr.

——2011, Assessment report describing diamond drilling at the Rau trend: Prepared for ATAC Resources Ltd., http://virtua.gov.yk.ca:8080/lib/item?id=chamo:168351&theme=emr.

Engebretson, D.C., Cox, A., and Gordon, R.G., 1985, Relative motions between oceanic and continental plates in the Pacific basins: Geological Society of America Special Paper, v. 206, p. 1–59.

Faure, G., and Mensing, T.M., 2005, Isotopes principles and applications: New Jersey, Wiley, p. 928.

Fonseca, A.L., 1998, Origin of carbonate hosted gold rich replacement deposits and related mineralization styles in the Ketza River deposit, Yukon Territory: Unpublished M.Sc. thesis, Vancouver, Canada, University of British Columbia, 108 p.

Gabrielse, H., 1967, Tectonic evolution of the northern Canadian Cordillera: Canadian Journal of Earth Sciences, v. 4, p. 271–298.

Glesemann, A., Jaeger, H.J., Norman, A.L., Krouse, H.R., and Brand, W.A., 1994, Online sulfur-isotope determination using an elemental analyzer coupled to a mass spectrometer: Analytical Chemistry, v. 66, p. 2816–2819.

Goldstein, R.H., and Reynolds, T.J., 1994, Systematics of fluid inclusions in diagenetic minerals: Society for Sedimentary Geology, Short Course 31, 199 p.

Goodfellow, W.D., Cecile, M.P., and Leybourne, M.I., 1995, Geochemistry, petrogenesis, and tectonic setting of lower Paleozoic alkalic and potassic volcanic rocks, northern Canadian Cordilleran miogeocline: Canadian Journal of Earth Sciences, v. 32, p. 1236–1254.

Gordey, S.P., and Anderson, R.G., 1993, Evolution of the northern Cordilleran miogeocline, Nahanni map area (1051), Yukon and Northwest Territories: Geological Survey of Canada, Memoir 428, 214 p.

Gordey, S.P., and Makepeace, A.J., 2001, Bedrock geology, Yukon Territory: Geological Survey of Canada, Open File 3754, Exploration and Geological Services Division, Yukon Indian and Northern Affairs Canada, Open File 2001-1, scale 1: 1,000,000, 2 sheets.

Gordey, S.P., Geldsetzer, H.H.J., Morrow, D.W., Bamber, E.W., Henderson, C.M., Richards, B.C., McGugan, A., Gibson, D.W., and Poulton, T.P., 1991, Ancestral North America; Upper Devonian to Middle Jurassic assemblages, chapter 8, in Gabrielse, H., and Yourath, C.J., eds., Geology of the Cordilleran orogeny in Canada: Ottawa, Ontario, Geological Survey of Canada, p. 221–329.

Hart, C.J.R., 2007, Reduced intrusion-related gold systems: Geological Association of Canada, Mineral Deposits Division, Special Publication No. 5, p. 95–112.

Hart, C.J.R., Goldfarb, R.J., Lewis, L.L., and Mair, J.L., 2004, The Northern Cordilleran mid-Cretaceous plutonic province: Ilmenite/magnetite-series granitoids and intrusion-related mineralisation: Resource Geology, v. 54, p. 253–280.

Heinrich, C.A., Gunther, D., Audetat, A., and Ulrich, T., 1999, Metal fractionation between magmatic brine and vapor, determined by microanalysis of fluid inclusions: Geology, v. 27, p. 755–758.

Hudson, T.L., 1994, Crustal melting events in Alaska, in Plafker, G., and Berg, H.C., eds., The geology of Alaska: Boulder, Colorado, Geological Society of America, Decade of North American Geology, v. G-1, p. 657–671.

Ishihara, S., 1977, The magnetite-series and ilmenite-series granitic rocks: Mining Geology, v. 27, p. 293–305.

——2004, The redox state of granitoids relative to tectonic setting and Earth history: The magnetite-ilmenite series 30 years later, Transactions of the Royal Society of Edinburgh: Earth Sciences, v. 95, p. 23–33.

Ishihara, S., Hashimoto, M., and Machida, M., 2000, Magnetite/ilmenite-series classification and magnetic susceptibility of the Mesozoic-Cenozoic batholiths in Peru: Resource Geology, v. 50, p. 123–129.

Kingston, S., Mortensen, J.K., Dumala, M., and Gabites, J., 2010, Ar-Ar geochronology and Pb isotopic constraints on the origin of the Rau gold-rich carbonate replacement deposit, central Yukon, in MacFarlane, K.E., Weston, L.H., and Blackburn, L.R., eds., Yukon exploration and geology 2009: Whitehorse, Yukon, Yukon Geological Survey, p. 213–222.

Lang, J.R., and Baker, T., 2001, Intrusion-related gold systems: The present level of understanding: Mineralium Deposita, v. 36, p. 477–489.

Leslie, C.D., 2009, Detrital zircon geochronology and rift-related magmatism: Central Mackenzie Mountains, Northwest Territories: Unpublished M.Sc. thesis, Vancouver, Canada, University of British Columbia, 162 p.

Lowenstern, J.B., 2001, Carbon dioxide in magmas and implications for hydrothermal systems: Mineralium Deposita, v. 36, p. 490–502.

Lynch, J.V.G., Longstaffe, F.J., and Nesbitt, B.E., 1990, Stable isotopic and fluid inclusion indications of large-scale hydrothermal paleoflow, boiling, and fluid mixing in the Keno Hill Ag-Pb-Zn district, Yukon Territory, Canada: Geochimica et Cosmochimica, v. 54, p. 1045–1059.

Mair, J.L., Goldfarb, R.J., Johnson, C.A., Hart, C.J.R., and Marsh, E.E., 2006a, Geochemical constraints on the genesis of the Scheelite dome intrusion-related gold deposit, Tombstone gold belt, Yukon, Canada: Economic Geology, v. 101, p. 523–553.

Mair, J.L., Hart, C.J.R., and Stephens, J.R., 2006b, Deformation history of the northwestern Selwyn Basin, Yukon, Canada: Implications for orogen evolution and mid-Cretaceous magmatism: GSA Bulletin, v. 118, p. 304–323.

Maloof, T., Baker, T., and Thompson, J., 2001, The Dublin Gulch intrusion-hosted gold deposit, Tombstone plutonic suite, Yukon Territory, Canada: Mineralium Deposita, v. 36, p. 583–593.

Marsh, E.E., Goldfarb, R.J., Hart, C.J.R., and Johnson, C.A., 2003, Geology and geochemistry of the Clear Creek intrusion-related gold occurrences, Tintina Gold Province, Yukon, Canada: Canadian Journal of Earth Sciences, v. 40, p. 681–699.

Moore, R.C., Lalicker, C.G., and Fischer, A.G., 1952, Invertebrate fossils: New York, McGraw-Hill, 738 p.

Morrow, D.W., Dubord, M.P., Uyeno, T.T., Norris, A.W., and Norford, B.S., 1999, Lower Paleozoic stratigraphy of northern Yukon Territory and northwestern District of Mackenzie: Geological Survey of Canada Bulletin 538, 202 p.

Mortensen, J.K., 1992, Pre-mid-Mesozoic tectonic evolution of the Yukon-Tanana terrane, Yukon and Alaska: Tectonics, v. 11, p. 836.

Moynihan, D., 2013, Bedrock geology of NTS 106B/04, eastern Rackla Belt: Whitehorse, Yukon, Yukon Exploration and Geology, p. 147–167.

Murphy, D.C., 1997, Geology of the McQuesten River Region, northern McQuesten and Mayo map area, Yukon Territory (115P/14, 15, 16; 105M/13, 14): Yukon, Exploration and Geological Services Division, Indian and Northern Affairs Canada, Bulletin 6, 122 p., http://data.geology.gov.yk.ca/Reference/DownloadProduct/17681.

Narbonne, G.M., and Aitken, J.D., 1995, Neoproterozoic of the Mackenzie Mountains, northwestern Canada: Precambrian Research, v. 73, p. 101–121.

Roedder, E., 1984, Fluid inclusions: Reviews in Mineralogy, v. 12, 646 p.

Rye, R.O., and Ohmoto, H., 1974, Sulfur and carbon isotopes and ore genesis: A review: Economic Geology, v. 69, p. 826–842.

Stephens, J.R., Mair, J.L., Oliver, N.H.S., Hart, C.J.R., and Baker, T., 2004, Structural and mechanical controls on intrusion-related deposits of the Tombstone gold belt, Yukon, Canada, with comparisons to other vein-hosted ore-deposit types: Journal of Structural Geology, v. 26, p. 1025–1041.

Sterner, S.M., Hall, D.L., and Bodnar, R.J., 1988, Synthetic fluid inclusions. V. Solubility relations in the system NaCl-KCl-H_2O under vapor-saturated conditions: Geochimica et Cosmochimica Acta, v. 52, p. 989–1005.

Stroshein, R., 1996, Geology and gold deposits at Ketza River, Yukon Territory, a progress report: Yukon Exploration and Geology, p. 43–48, http://data.geology.gov.yk.ca/Reference/DownloadProduct/16969.

Stroshein, R.W., Giroux, G.H., and Wengzynowski, W.A., 2011, Technical report using National Instrument 43-101 guidelines for the preparation of the Tiger deposit mineral resource estimate on the Rau property Yukon Territory, Canada NTS map sheets 106D 01/06/07/08 latitude 64° 11' N longitude 134° 22': Prepared for ATAC Resources Ltd., 113 p., http://www.atacresources.com/projects/technical-reports.

Thompson, J.F.H., Sillitoe, R.H., Baker, T., Lang, J.R., and Mortensen, J.K., 1999, Intrusion-related gold deposits associated with tungsten-tin provinces: Mineralium Deposita, v. 34, p. 323–334.

Tucker, M.J., 2015, Geology, mineralization and geochronology of the Conrad zone Carlin-type prospect, east-central Yukon Territory, Canada: Unpublished M.Sc. thesis, Vancouver, Canada, University of British Columbia, 235 p.

Turner, F.J., Griggs, D.T., and Heard, H.C., 1954, Plastic deformation of dolomite rock at 380ºC: American Journal of Science, v. 252, p. 477–488.

Valley, J.W., 1986, Stable isotope geochemistry of metamorphic rocks: Reviews in Mineralogy and Geochemistry, v. 16, p. 445–489.

Veizer, J., Ala, D., Azmy, K., Bruckschen, P., Buhl, D., Bruhn, F., Carden, G.A.F., Diener, A., Ebneth, S., Godderis, Y., Jasper, T., Korte, C., Pawellek, F., Podlaha, O.G., and Strauss, H., 1999, $^{87}Sr/^{86}Sr$, $\delta^{13}C$ and $\delta^{18}O$ evolution of Phanerozoic seawater, Chemical Geology, v. 161, p. 59–88.